University of Crete

MSc thesis

Study of the magnetic field and filamentary structures in the Polaris Flare molecular cloud

Author:
Ioanna Psaradaki

Supervisor:
Professor Konstantinos Tassis

July 18, 2016

Study of the magnetic fields and filamentary structures in the Polaris Flare molecular cloud

Abstract: In diffuse molecular clouds, possible precursors of star-forming clouds, the effect of the magnetic field is unclear. In this thesis we compare the orientations of filamentary structures in the Polaris Flare, as seen through dust emission by *Herschel*, to the plane-of-the-sky magnetic field orientation (B_{pos}) as revealed by stellar optical polarimetry with RoboPol. Dust structures in this translucent cloud show a strong preference for alignment with B_{pos}. 70% of field orientations are consistent with those of the filaments (within 30°). We also explore the spatial variation of the relative orientations and find it to be uncorrelated with the dust emission intensity and correlated to the dispersion of polarization angles.

Μελέτη του μαγνητικού πεδίου και των νηματοειδών δομών στο μοριακό νέφος Polaris Flare.

Περίληψη: Σκοπός της παρούσας διπλωματικής εργασίας είναι η μελέτη του μαγνητικού πεδίου στις νηματοειδείς δομές που παρατηρούνται σε νέφη μοριακού υδρογόνου στο μεσοαστρικό χώρο. Συγκεκριμένα ασχολούμαστε με το μοριακό νέφος χαμηλής πυκνοτητας αερίου Polaris Flare. Το Polaris Flare δεν παρουσιάζει ενεργή αστρογέννεση συνεπώς είναι ένα καλό παράδειγμα για τη μελέτη των αρχικών συνθηκών που αφορούν την αστρογέννεση. Ο ρόλος του μαγνητικού πεδίου στην αστρογέννεση είναι ακόμα ασαφής. Αρχικά συγκρίνουμε τη διεύθυνση των νηματοειδών δομών που έχουν παρατηρηθεί στο υπέρυθρο απο το διαστημικό τηλεσκόπιο Herschel με το μαγνητικό πεδίο στο επίπεδο του ουρανού όπως παρατηρήθηκε απο το οπτικό πολωσίμετρο Robopol του Αστεροσκοπείου του Σκίνακα στην Κρήτη. Τα αποτελέσματα έδειξαν ότι το μαγνητικό πεδίο στο επίπεδο του ουρανού τείνει να ευθυγραμμίζεται με τις νηματοειδείς δομές του νέφους συνεπώς το μαγνητικό πεδίο επηρρεάζει σημαντικά την κίνηση του αερίου στο σύννεφο. Επιπλέον μελετήθηκε η διακύμανση της σχετικής διεύθυνσης μεταξύ του μαγνητικού πεδίου και των νηματοειδών δομών κατά μήκος όλου του πεδίου παρατήρησης καθώς και άλλων μεγεθών όπως ο βαθμός πόλωσης και η ένταση της σκόνης στο υπέρυθρο.

Acknowledgments

I would like to express my gratitude to my supervisor K. Tassis, for his patient mentoring and enthusiastic encouragement on this research work. I am also grateful to professors V. Pavlidou and N. Kylafis for their useful critiques.

I would like to appreciate G.V. Panopoulou for her guidance throughout the entire project as well as for providing FilTER code used in this thesis. I also thank D. Clemens, S. Clark and E. Koch for helpful advice and for releasing their algorithms for public use.

I would like to acknowledge A. Tritsis, D. Blinov, J. Liodakis, R. Skalidis and E. Palaiologou for their help throughout the duration of this project.

This research has used data from RoboPol project and the Herschel Gould Belt Survey (HGBS) project (http://gouldbelt-herschel.cea.fr).

Contents

Chapter 1

Introduction

Today we know that space between stars is not empty. It contains gas (mostly hydrogen), dust grains, cosmic rays and it is permeated by magnetic fields and photons. All these components compose the *interstellar medium (ISM)*. The ISM does not have a uniform density. It contains cold regions with temperatures around 10 K and is dominated by molecular hydrogen. These regions are refereed to as *interstellar molecular clouds*. Into these regions new stars are born.

After recent Herschel space telescope observations new information about the structure of molecular clouds was revealed. Herschel found a network of elongated structures in every molecular cloud. These structures are called filaments (Fig. 1.1). The Gould Belt Survey conducted by the *Herschel* space observatory captured the morphologies of the nearby molecular clouds with unprecedented sensitivity and detail, allowing the study of filamentary structures to advance [André et al. , 2010]. Moreover, the filamentary structures of the cold ISM must be closely related to the star formation process since more than 70% of the prestellar cores identified with Herschel in nearby clouds appear to lie within filaments (Fig. 1.2). It has been suggested that prestellar dense cores form primarily along filaments [Men'shchikov et al., 2010]. Today it is believed that filaments may form into the parent cloud and then break up into cores.

Arzoumanian et al. [2011] found that these filaments have a characteristic width at 0.1 pc. This is illustrated in Fig. 1.3 which shows that nearby interstellar filaments are characterized by a very narrow distribution of inner FWHM widths centred at about 0.1 pc. The origin of this quasi-universal width of interstellar filaments is not yet well understood. A possible interpretation is that the filament width at 0.1 pc is comparable to the cutoff of MHD waves in (low-density, primarily neutral) molecular clouds [Mouschovias , 1991, Hennebelle , 2013]. Another possibility is that it corresponds to the sonic scale below which interstellar turbulence becomes subsonic in diffuse, non-star-forming molecular gas [Padoan et al. , 2001].

1.1 The magnetic field

It is important to answer whether the magnetic field interacts with filaments and how this interaction takes place. Its role in the various stages and environments of star formation is hotly debated. Observations showed that the magnetic field tend to be perpendicular to dense filaments and parallel to faint ones (Fig. 1.4).

In simulations of super-Alfvénic turbulence, magnetic fields are tangled due to the gas flow [Ostriker, Stone, & Gammie , 2001]. In such models, filaments are formed by shock interactions and the magnetic field within them is found to lie along their spines. In studies of sub/trans-Alfvénic turbulence, where the magnetic field is dynamically important, filament orientations with respect to the large scale ordered field, depend on whether gravity is important. In simulations where gravity is not taken into account or structures are gravitationally unbound [Soler et al. , 2013], filaments are parallel to the magnetic field. On the other hand, self-gravitating elongated structures are perpendicular to the magnetic field [Mouschovias , 1976]. Both configurations are the result of the magnetic force facilitating flows along field lines.

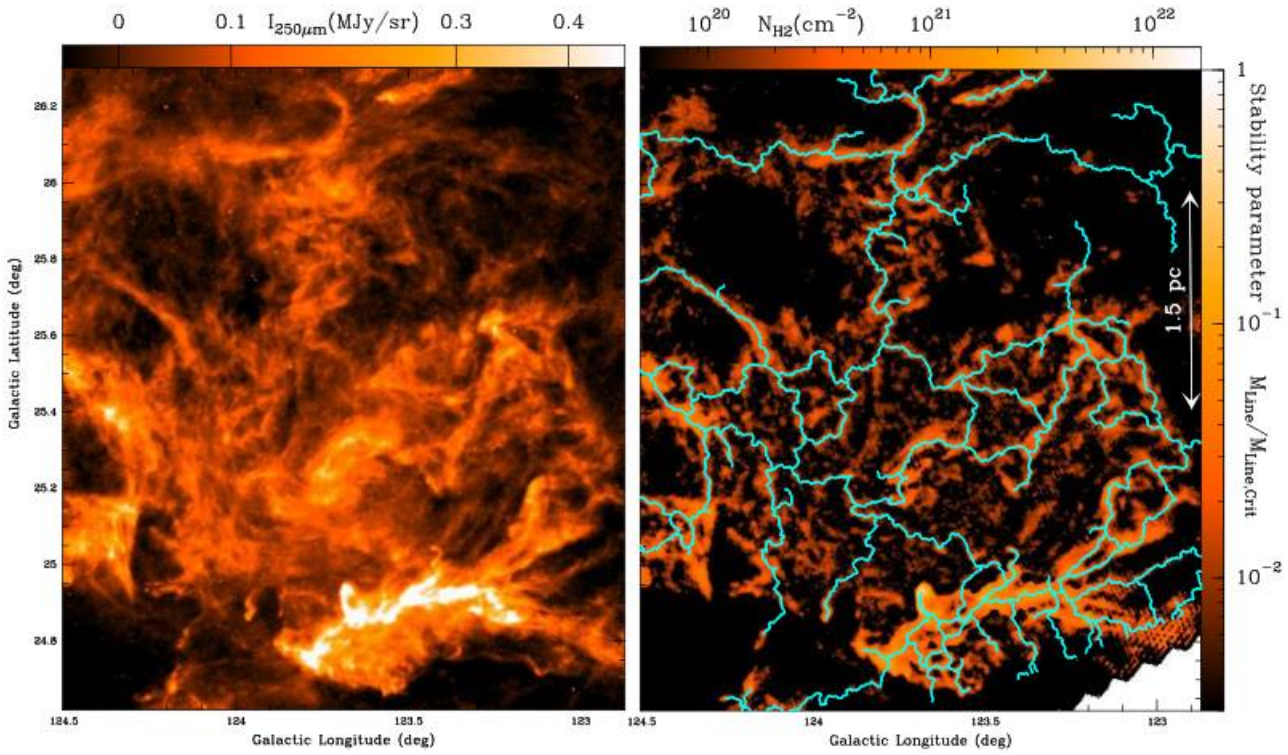

Figure 1.1: Left: Herschel SPIRE dust continuum map of a portion of the Polaris Flare. Right: Corresponding column density map derived from Herschel data. The skeleton of the filament network identified with the DisPerSE algorithm [Sousbie , 2011] is shown in light blue [André et al. , 2013].

Finally, if the magnetic field surrounding a filament has a helical configuration Fiege & Pudritz [2002] the relative orientation of the two as projected on the plane of the sky can have any value, depending on projection, curvature and if the field is mostly poloidal or toroidal [Matthews , 2001].

1.1.1 Measuring the plane-of-the-sky magnetic field

The presence of dust allows us to study the magnetic field in these structures. Observationally we measure the plane-of-the-sky magnetic field with optical stellar polarization (see Fig. 1.5). The idea is that the unpolarized light coming from the star behind the cloud propagates through the cloud. Into the molecular cloud dust grains act as a polaroid. They absorb the component of the light which is parallel to their long axis and they re-emit it thermally in the far-infrared. The remaining light is transmitted and it is partially polarized in the direction of the magnetic field. This is the polarization (or the plane-of-the-sky magnetic field) observed in the optical [Andersson, Lazarian & Vaillancourt , 2015].

Observational studies find increasing evidence that the cloud structure and magnetic field are closely related to each other. On cloud scales, Li et al. [2013] found that the distribution of relative orientations of filaments and the magnetic field (both projected on the plane of the sky) is bimodal: clouds either tend to be parallel or perpendicular (in projection) to the magnetic field. In a series of papers the *Planck* collaboration compared the magnetic field to ISM structure across a range of hydrogen column densities (N_H). Planck Collaboration Int. XXXII [2014] considered the orientation of structures in the diffuse ISM in the range of $N_H \sim 10^{20} - 10^{22}$ and found significant alignment with the plane-of-the-sky magnetic field (B_{pos}). Planck Collaboration Int. XXXV [2015] found that in their sample of 10 nearby clouds, substructure at high column density tends to be perpendicular to the magnetic field, whereas at low column density there is a tendency for alignment.

Studies of optical and NIR polarization, tracing B_{pos} in cloud envelopes, show that dense filaments within star-forming molecular clouds tend to be perpendicular to the magnetic field. On the other

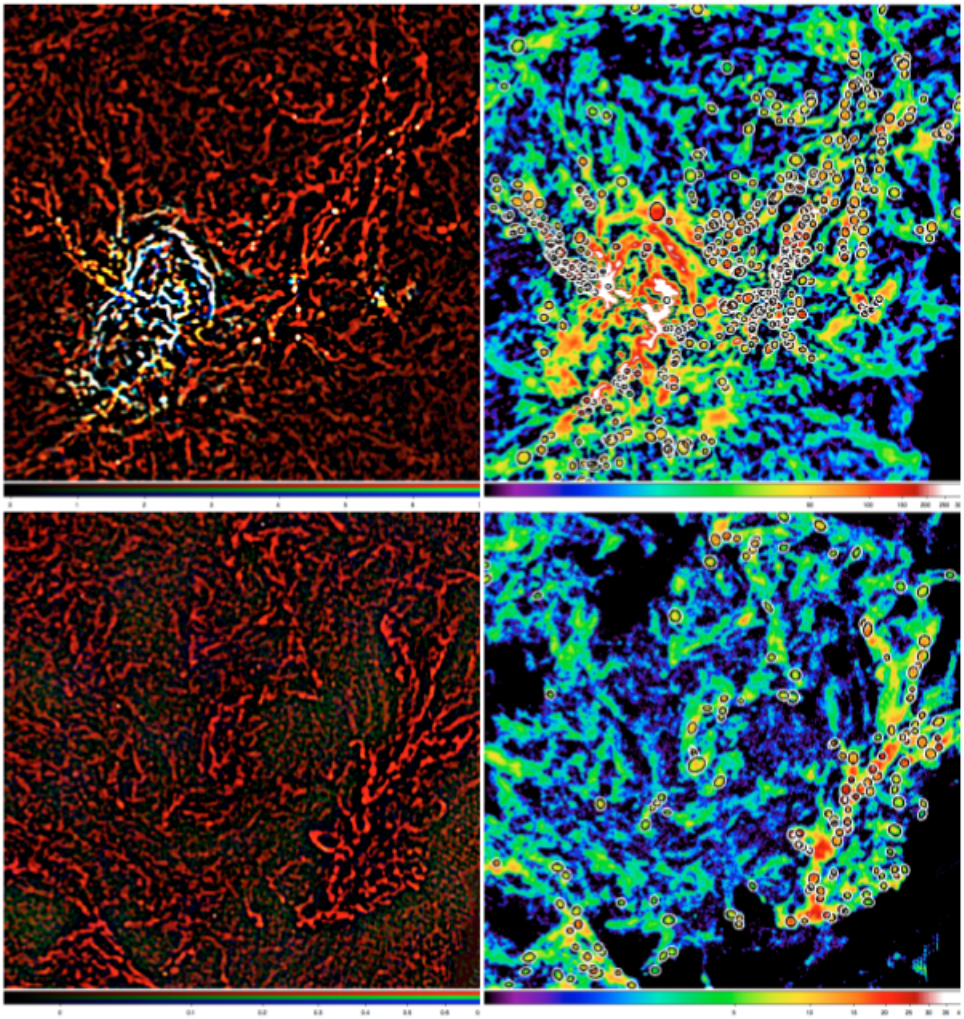

Figure 1.2: Left: Composite 3-color images left of the sub-fields of Aquila (top) and Polaris (bottom). Right: Starless cores extracted from the original data[Men'shchikov et al., 2010].

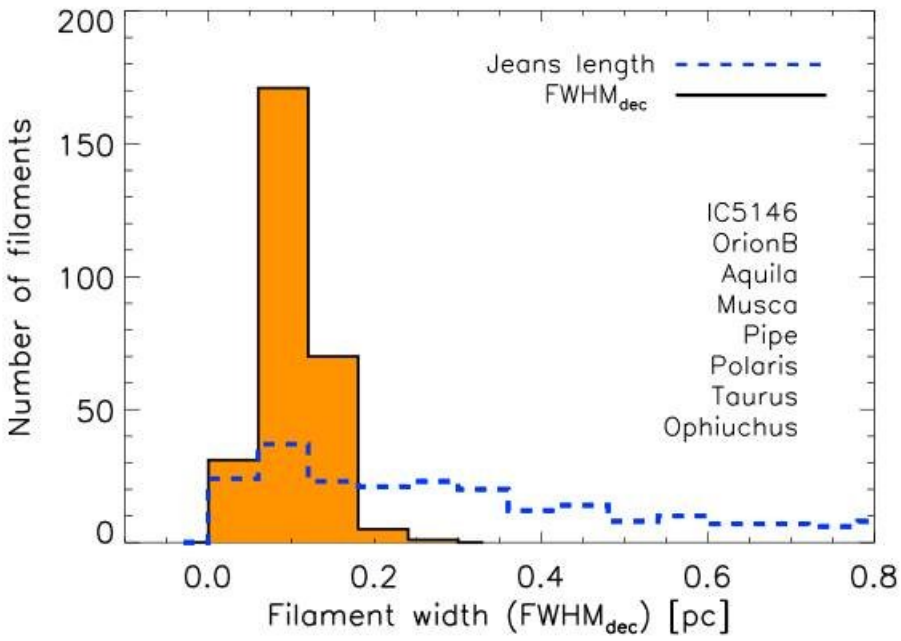

Figure 1.3: Histogram of deconvolved FWHM widths for a sample of 278 filaments in 8 nearby regions of the Gould Belt survey [Arzoumanian et al. , 2011].

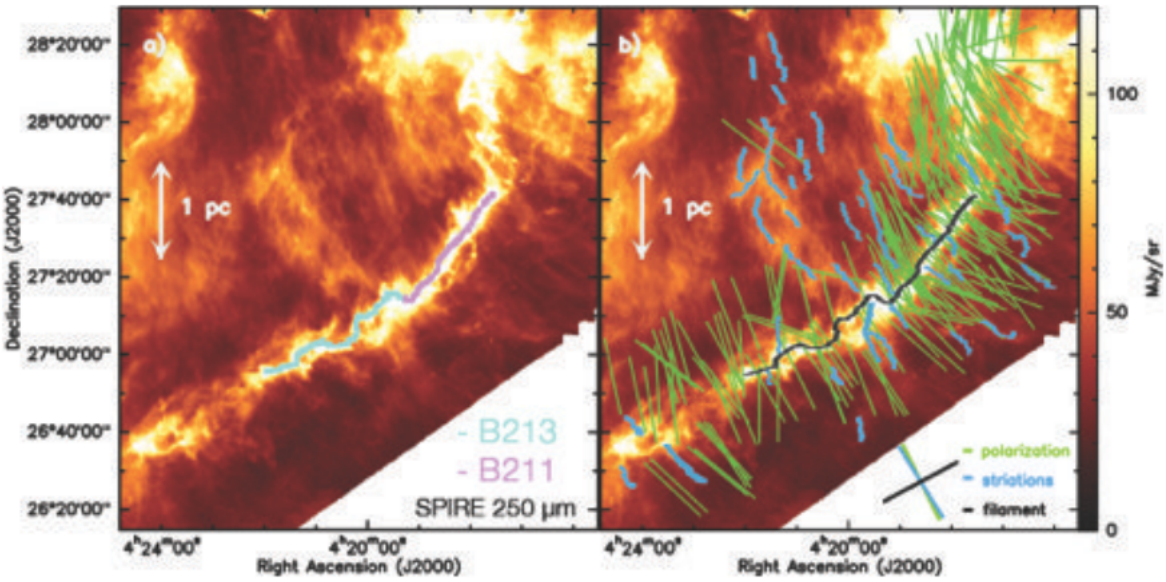

Figure 1.4: (a) Herschel/SPIRE hildebrand250 μ m dust continuum image of the B211/B213/L1495 region in Taurus (d $\sim$ 140 pc).(b) Display of optical and infrared polarization vectors from (Chapman et al. [2011] tracing the magnetic field orientation in the same region, overlaid on the Herschel/SPIRE 250 μ m image [Palmeirim et al. , 2013].

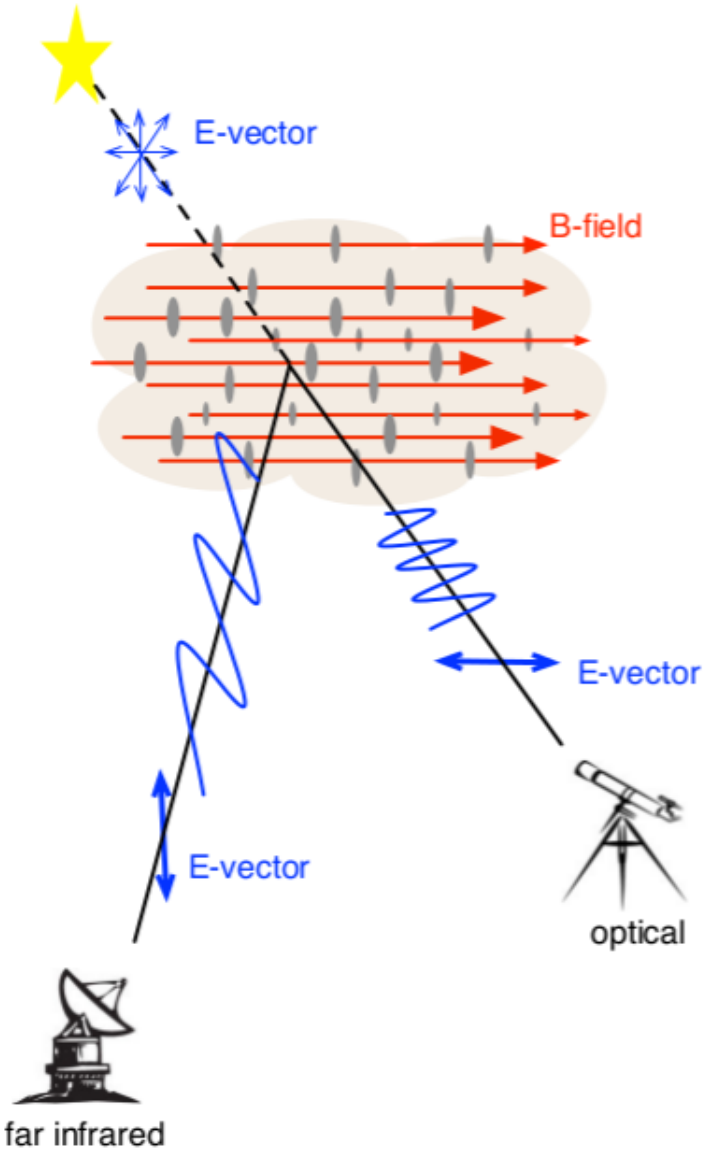

Figure 1.5: Linear polarization in molecular cloudsTassis K. [2014]

hand, there are diffuse linear structures termed *striations*, that share a common smoothly varying orientation and are situated either in the outskirts of clouds [Goldsmith et al. , 2008, Alves de Oliveira et al. , 2014] or near dense filaments [Palmeirim et al. , 2013]. These structures show alignment with B_{pos} [Chapman et al. , 2011, Palmeirim et al. , 2013, Alves de Oliveira et al. , 2014, Malinen et al., 2015].

Chapter 2

Data: The Polaris Flare

While the large-scale magnetic field has been mapped in many dense molecular clouds, little is known about the field in diffuse molecular clouds. In this work we study the Polaris Flare. The Polaris Flare is a high-latitude diffuse cloud located at a distance 140 - 240 pc (this number is still debated). The Polaris Flare is in the early stages of star formation with any signs of active star formation [André et al. , 2010] except for the existence of possibly prestellar core(s) in the densest part of the cloud MCLD 123.5+24.9 (MCLD123) [Ward-Thompson et al. , 2010, Wagle et al. , 2015] so it is a good environment to examine the initial conditions of star formation. For the purposes of this project we used cross-correlated Herschel dust emission maps and magnetic field directions in the Polaris Flare using polarimetric data from RoboPol.

Herschel dust emission data

The dust emission in $\sim$16 deg^2 of the Polaris Flare has been mapped by as part of the *Herschel* Gould Belt Survey. This map (Fig.2.1) reveals for the first time the structure of the diffuse interstellar medium on scales ranging from 0.01 to 8 pc [Miville-Deschênes et al. , 2010]. The Polaris Flare dark cloud region was observed with both PACS and SPIRE on Herschel at five wave-lengths – 70, 160, 250, 350 and 500 μm. We used the image taken at 250 μm.

Optical polarization measurements with RoboPol

The *Planck* space observatory has provided the first map of the plane-of-the-sky magnetic field in the area at tens of arcminute resolution. In Figure 2.2 the map of the plane-of-the-sky magnetic field in the same area, measured by stellar optical polarimetry with RoboPol is presented [Panopoulou et al., 2015]. RoboPol is a wide-field polarimeter mounted on the 1.3 meter telescope at Skinakas Observatory in Crete. The Polaris Flare was the first interstellar medium region mapped with RoboPol.

The resolution of optical polarimetry (pencil beams) and coverage of our data allow for a detailed comparison between magnetic field and cloud structure.

The goal of this thesis is to compare the magnetic field orientation to that of the linear structures in the Polaris Flare. We present the distribution of relative orientations of filaments and B_{pos} throughout the mapped region. We compare properties such as the relative orientations and polarization angle dispersion across the map and present the distribution of filament widths.

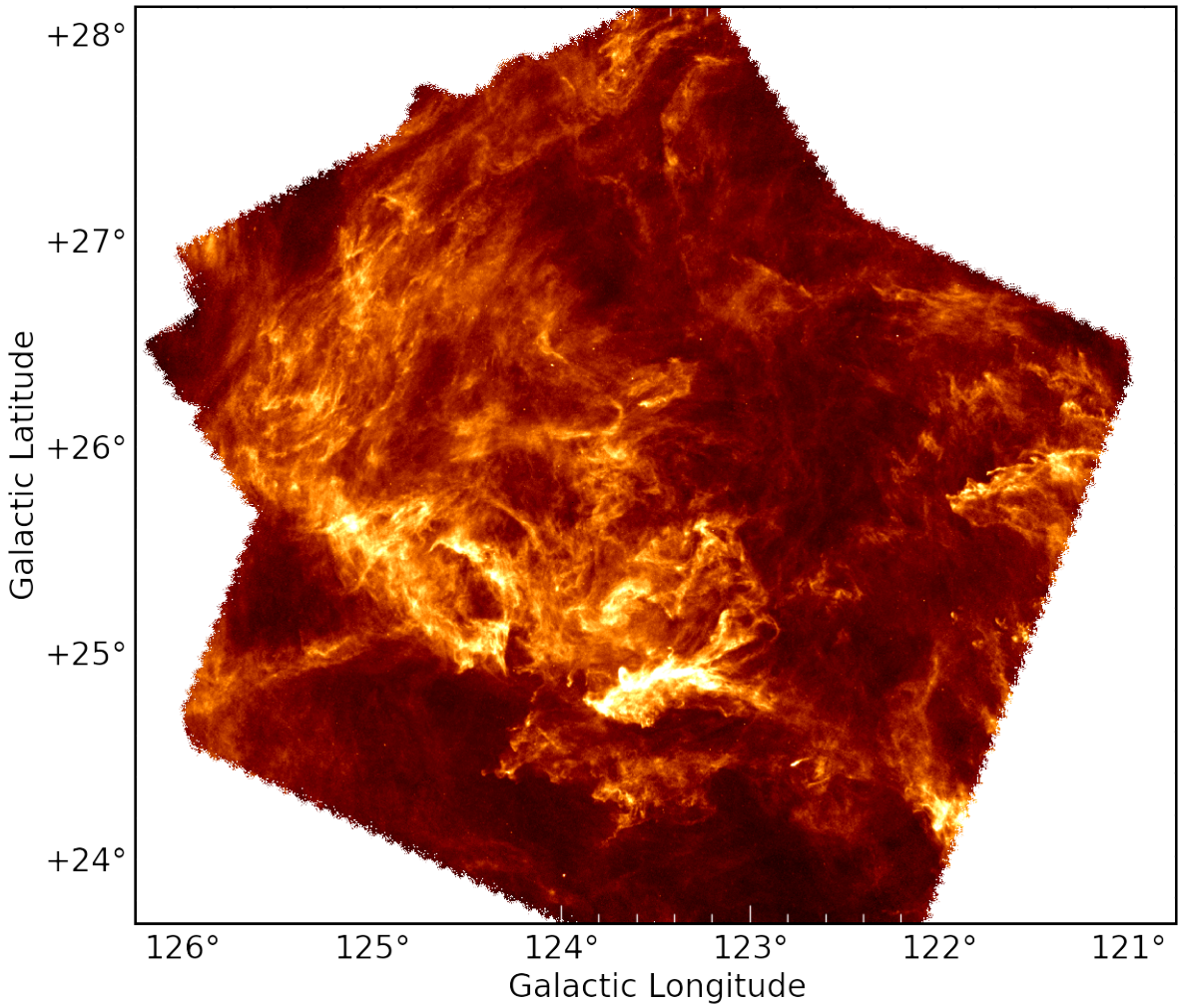

Figure 2.1: The Polaris Flare, Herschel dust emission map, 250 μ m by André et al. [2010]

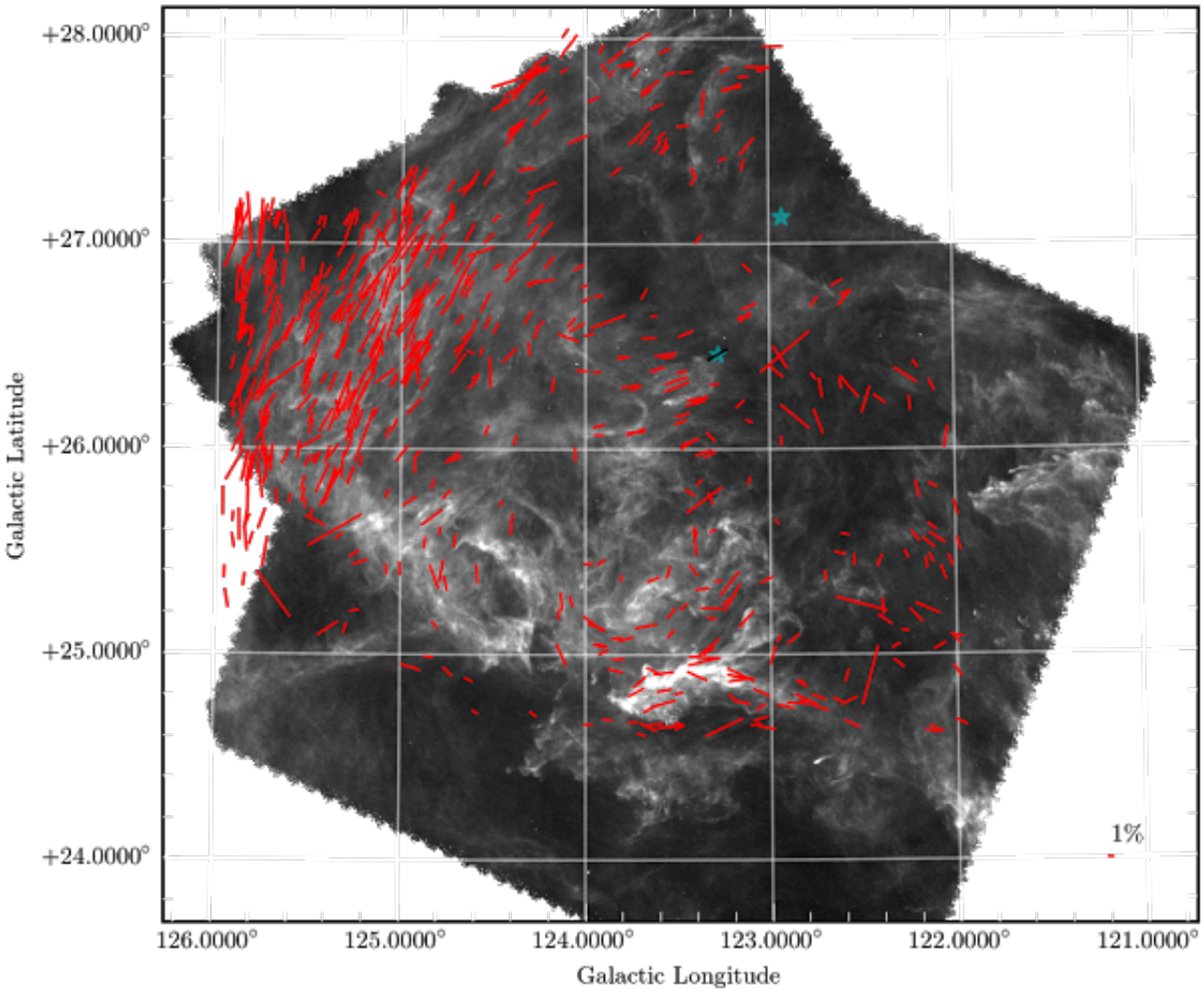

Figure 2.2: The Polaris Flare with polarization measurements (red segments) by Panopoulou et al. [2015]

Chapter 3

Algorithms

3.1 The Rolling Hough Transform

An excellent tool for determining the orientation of linear structures, irrespective of their brightness, is the Rolling Hough Transform (RHT) [Clark et al. , 2014]. It was introduced in the study of diffuse HI and has been used in analyses of molecular clouds as well [Koch & Rosolowsky, 2015, Malinen et al., 2015]. The Rolling Hough Transform, as its name indicates, is a modification of Hough Transform. The Hough transform is a feature extraction technique used in image analysis, computer vision, and digital image processing. A rolling version of Hough Transform is used in this algorithm for the detection and quantization of linear features in astronomical data.

The RHT returns the probability that a pixel is part of a linear structure as a function of angle. By integrating over all angles we produce the RHT output R(x,y).

$$R\left(x,y\right)=\int R\left(\theta,x,y\right)d\theta \tag{3.1}$$

Parameter space

The RHT uses three parameters to create the backprojection image, a smoothing kernel of diameter Dk, a window of diameter Dw and an intensity threshold Z. The window of diameter Dk rolls across the data and is centered on each pixel. Linear structures at least as long as Dw will be identified. Threshold Z is a lower limit of the linear probability. Over this threshold coherent structures are identified. In figure 3.3 we present the backprojection image of a part of the Polaris Flare (Figure 3.2) using the Rolling Hough Transform.

3.1.1 Relative orientation of filaments and magnetic filed

In most cases, it is significant to examine the difference of the polarization segments and the filaments direction. The Rolling Hough transform can give a value of the filament angle. Thus we can obtain a quantified result of the angle difference between the filaments and the magnetic field. The RHT gives the value of R(θ, x, y), which is a value of intensity as a function of angle. In the beginning we sum all the R values in a circular region (considered as the fourth parameter) around each star in the field.

$$R_{*}(\theta)=\iint_{disk}R(\theta,x,y)dxdy \tag{3.2}$$

R_{*} is an one-dimensional matrix in which, each element represents the sum of all the angles that the circular region contains. Then we compute the angle as follows,

$$\langle\theta_{RHT}\rangle^{'}=\frac{1}{2}arctan\left[\frac{\int sin(2\theta)R_{*}(\theta)d\theta}{\int cos(2\theta)R_{*}(\theta)d\theta}\right] \tag{3.3}$$

Finally we find the equivalent value in the interval $\theta\epsilon(0,\pi]$.

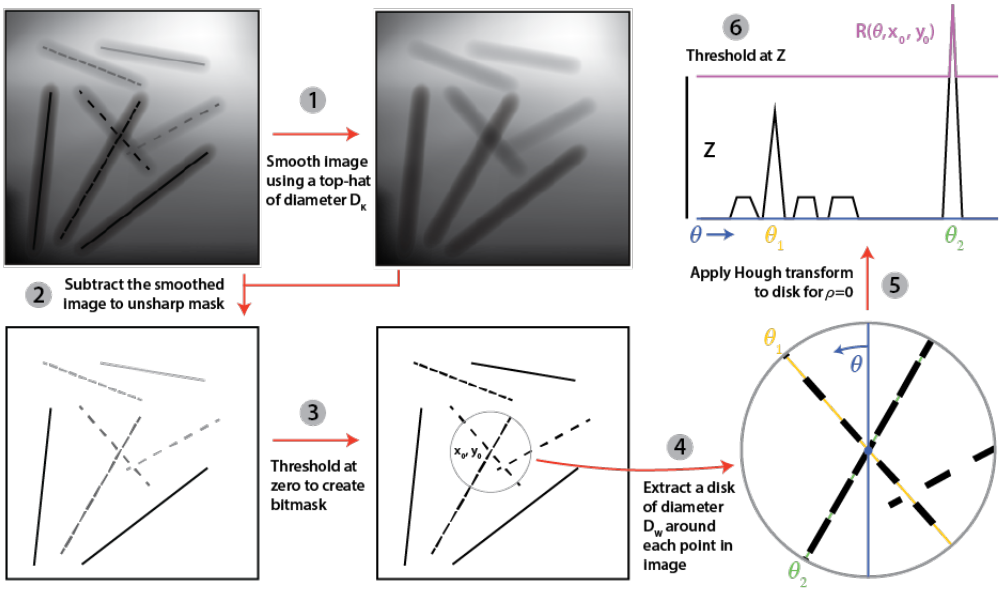

Figure 3.1: A diagram of the RHT procedure Clark et al. [2014]

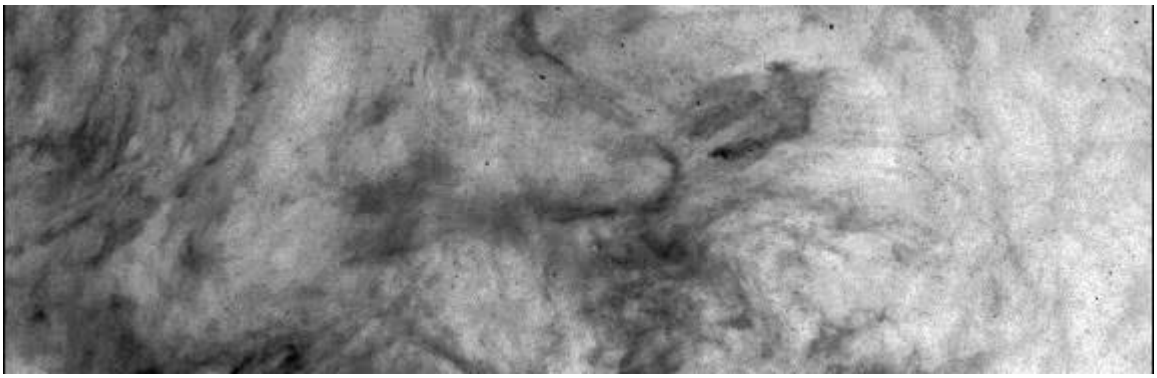

Figure 3.2: A part of the Polaris Flare used as input to the Rolling Hough Transform

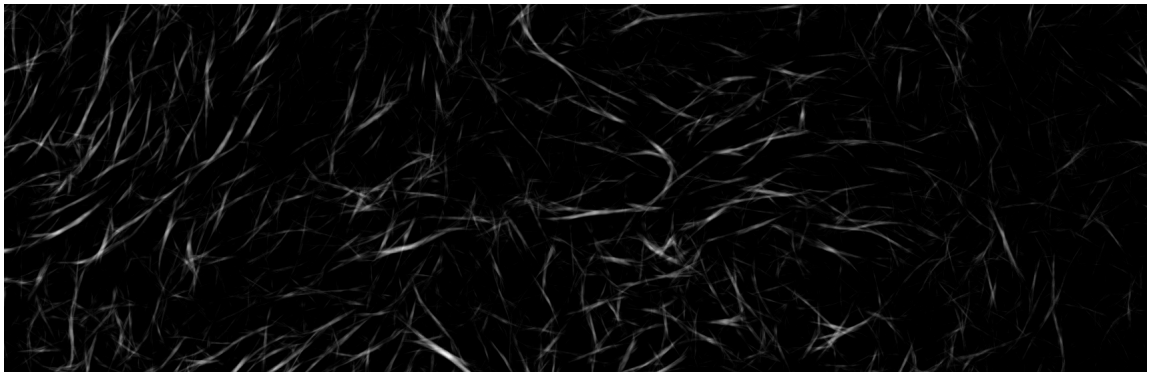

Figure 3.3: Filamentary structures identified by the Rolling Hough Transform as a result of the input image presented in Figure 3.2

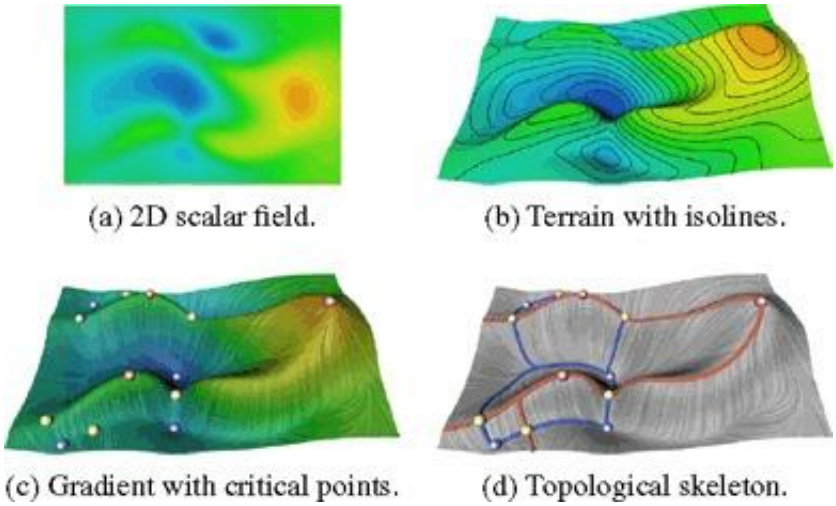

Figure 3.4: A simple 2D scalar function. Critical points are depicted as dots. Minima are shown in blue, maxima in red, saddles in yellow. The red and blue lines are the (ascending and descending) arcs of the skeleton [Weinkauf and D. Gunther , 2009].

$$\langle \theta_{RHT} \rangle = \pi - mod(\langle \theta_{RHT} \rangle^{'} + \pi, \pi) \tag{3.4}$$

This value represents a measure of the orientation of the gas around each star. To find the angle difference between the polarization segments and the filament orientation we simply take the difference of the two values.

$$\langle \varphi_{RHT} \rangle = \langle \theta_{RHT} \rangle^{'} - \theta^{*} \tag{3.5}$$

If $\langle \varphi_{RHT} \rangle$ is zero it means that $R_{*}(\theta)$ is well aligned with its starlight polarization angle.

3.2 The DisPerSe software

DisPerSe (Discrete Persistent Structures Extractor) software is an open source software for the automatic identification of structures in 2D and 3D noisy data sets designed by Sousbie [2011]. The software is designed to identify all sorts of topological structures. Firstly, it was widely applied to cosmological simulations but it has also been used for filamentary structure extraction found in the interstellar medium.

Disperse software is based on discrete Morse Theory. It is designed to connect local maxima (cores). DisPerSe extracts the topological skeletons of a surface (see Figure 3.4). A topological skeleton can be defined as the smallest possible set of lines that preserve the topology. The basic concept of the topology is based on two quantities, the gradient and its flow. The lines that follow the direction of the gradient are called field lines. In figure (3.4) (c) are shown the critical points i.e. the points where the gradient vanishes. DisPerSe uses two main parameters to create the topological skeleton, persistence and robustness.

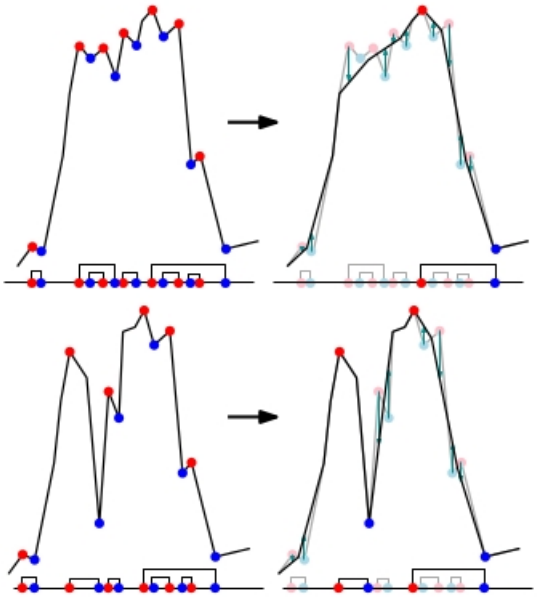

Figure 3.5: Simplification of topological skeleton using persistence. Left: function before simplification. Right: function after simplification. The diagram under each function represents its Morse-Smale complex and persistence pairs [Sousbie , 2011]

Persistence

Persistence represents the absolute difference of the intensity value between the two critical points in a persistence pair. Persistence is always positive and represents the importance of the topological feature defined by the persistence pair: low persistence pairs are sensitive to changes in the value of the function, and the corresponding critical points are easily destroyed, even by the introduction of noise in the function, while high persistence pairs are robust. Removing low persistence pairs from the Morse-Smale complex is a way to filter noise and non-meaningful structures (Figure 3.5).

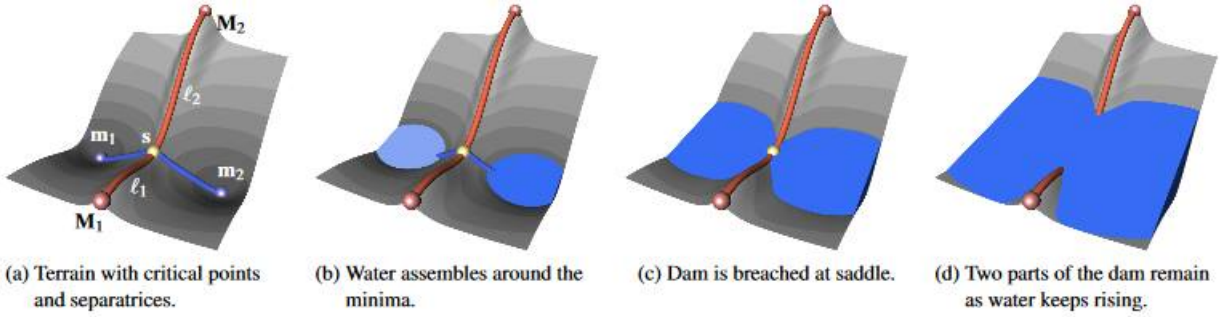

(a) Terrain with critical points and separatrices.

(b) Water assembles around the minima.

(c) Dam is breached at saddle.

(d) Two parts of the dam remain as water keeps rising.

Figure 3.6: Robustness threshold increasing towards the right. Linear structures entirely below that level vanish [Weinkauf and D. Gunther , 2009]

Robustness

Robustness is a continuous version of persistence which extends to filaments (persistence applies to pairs of critical points only). Robustness assigns an importance weight to each point along a filament. It respects that the importance of a feature may smoothly change along the line (Figure 3.6)

3.3 Filament Trait Evaluated Reconstruction method

An important morphological characteristic of filaments is their width. An excellent tool to determine the filament width is the Filament Trait-Evaluated Reconstruction (FilTER) designed by Panopoulou et al. [2014]. DisPerSe tends to connect structures that are not necessarily a whole. Filter provides a way to distinguish which filaments are really an entity. If along a filament there are gaps (e.g. profiles there were not peaked) the filament is not a single cylinder-like structure. The width of a filament can be provided by looking the cross- sections at different points along its length. A standard approach is to study the average of all profiles along it.

Filter choose to fit all profiles along a filament individually in order to examine the variation of the width along the filament. The algorithm performs what we call 'dynamical fitting'. It begins from a constant given profile extent, it fits Gaussians to smaller and smaller radii, removing two pixels on each side of the profile. It stops at a given extent, which is considered as minimal for bone widths. In our data this extend is set to 30 pixels corresponding to 0.12 pc.

Filter takes as an input the skeleton provided by disperse. Then the Gaussian is fit to the radial profile at every point along the filament axis, and the resulting FWHM is deconvolved by the beam size.

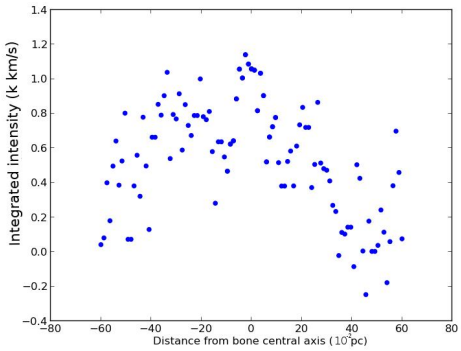

Figure 3.7: Inside noise level [Panopoulou et al. , 2014].

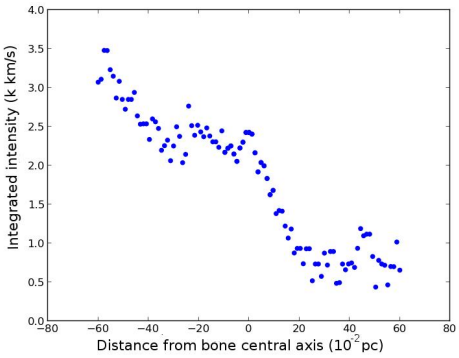

Figure 3.8: On the side of a real structur e[Panopoulou et al. , 2014].

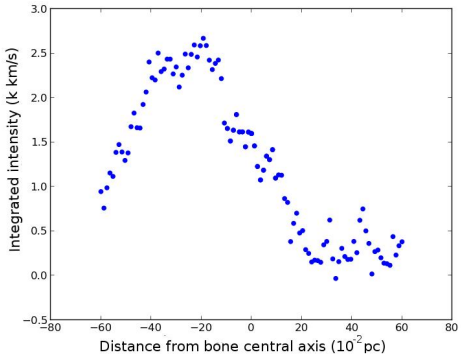

Figure 3.9: On the side of a real structure [Panopoulou et al. , 2014].

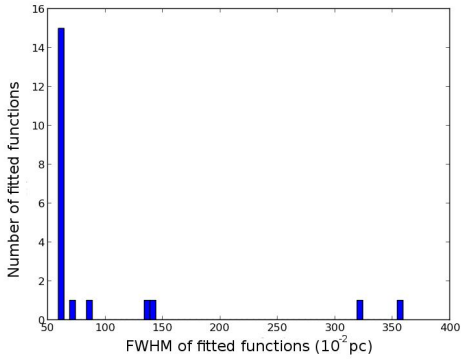

Figure 3.10: Distribution of FWHMs from dynamical fitting of profile c [Panopoulou et al. , 2014].

'Acceptable' and 'non acceptable' profiles

The result of the dynamical fitting process tests whether a profile is 'acceptable' or not. If the profile is smoothly peaked, the fits should be around the shape of the profile. This means that the mode of the FWHM distribution of the fits will be the one closest to reality. Otherwise, if the profile is one-sided the frequency of the mode should be 1, meaning no fit looks like the others. Profiles with these bad structure are shown in figures 3.7, 3.8, 3.9 and 3.10. In addition in figures 3.11, 3.12 we present a profile and the distribution of FWHMs that can be accepted as part of a real filamentary structure.

In general the criteria used to determine the quality of the profile are:
I. The frequency of the mode of the distribution of FWHMs must be larger than unity, i.e. the profile must have at least one peak.

II. The fit corresponding to the mode of FWHMs must have a mean within 7 pixels of the bone's central axis, i.e. the profile is centrally peaked.

III. The difference of the peak intensity of the last fit from the intensity value of the lowest point in the profile must be larger than the noise level.

The background (or noise) level is set as a rough estimate according to the values of the intensity of the image. In the Polaris Flare the noise level is set to 1.

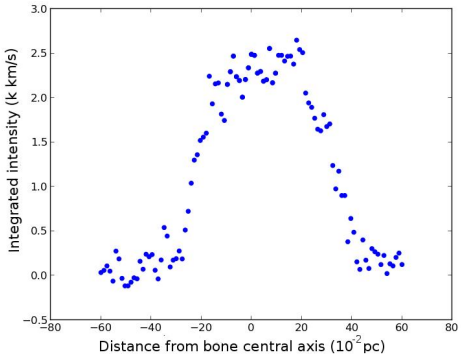

Figure 3.11: Example of a good profile [Panopoulou et al. , 2014]

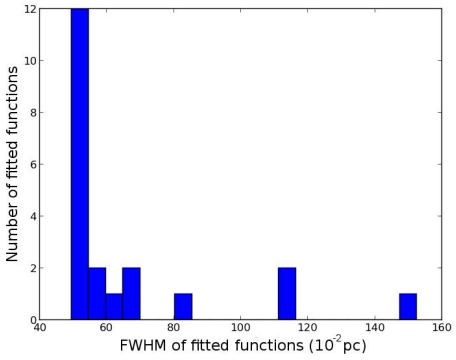

Figure 3.12: Distribution of FWHMs from dynamical fitting of profile on the left [Panopoulou et al. , 2014].

Chapter 4

Analysis of the integrated emission map of the Polaris Flare

4.1 Filament identification

We applied the Rolling Hough Transform to the Herschel dust emission map of the Polaris Flare at 250 μm and present the RHT backprojection. In figures 4.1, 4.2, 4.3, 4.4 we present the backprojection images produced with different parameters. The darkest pixels in the image belong to well-defined linear structures in intensity. The image for the analysis is presented in Figure 4.2 and it is produced with a intensity threshold (Z) of 0.75, a window of diameter (Dw) of 41 pixels and a smooth value (Dk) of 5. We also performed a parameter study and present it in section 4.3.

4.2 Relative orientations of Bpos and dust filaments

We combined the polarization data width the RHT output to provide the distribution of the relative orientation of the filaments and the plane-of-sky magnetic field. The polarization segments tracing the orientation of B_{pos} are overplotted in red (Figure 4.5). Regions A (striations) and B (MCLD123), indicated by the rectangles in the full map and are discussed in detail in Chapter 7.

At the position of each polarization measurement, we calculated the mean RHT angle, $\theta_{\rm RHT}$, within a circle of diameter 0.17 pc (corresponding to an angular diameter of 4 arcmin). We needed a circle diameter larger than the characteristic width of the filaments found Arzoumanian et al. [2011]. We then compared $\theta_{\rm RHT}$ to the orientation of each polarization segment, θ, by taking the absolute value of their difference[1], $|\theta - \theta_{\rm RHT}|$. There are 42 polarization measurements that extend outside the dust emission image and are not included in the comparison to cloud structures. The distribution of the relative orientations for the 590 remaining measurements is presented in Fig (4.6). There is a strong preference in alignment: 75% of polarization measurements are within 30 degrees of the orientation of linear features in their surrounding gas. A Monte-Carlo run showed that the probability of obtaining this correlation by chance is less than 10^{-6}. Only 11% are within 30 degrees of being perpendicular to their surrounding gas.

[1] All angles are defined with respect to the North and increase towards the East, according to the IAU convention.

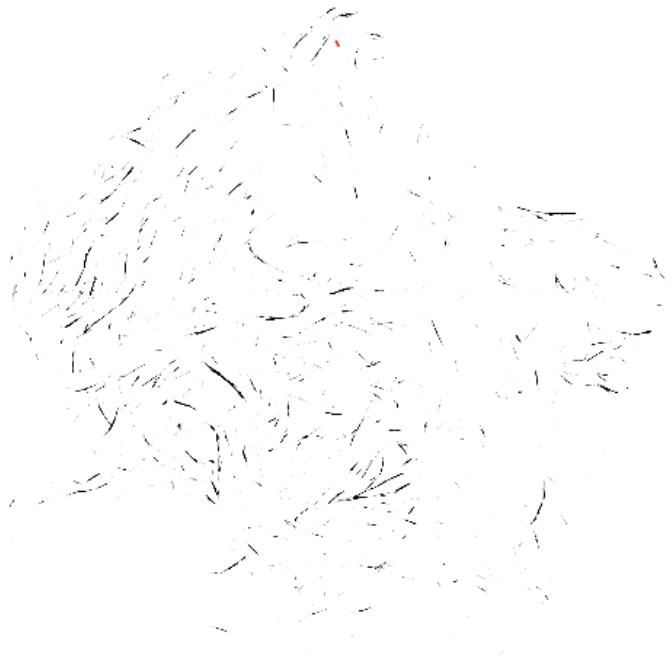

Figure 4.1: RHT visualization of the Herschel 250 μ m image of the Polaris Flare (grayscale) made with Z=0.9, Dw=77, Dk=15

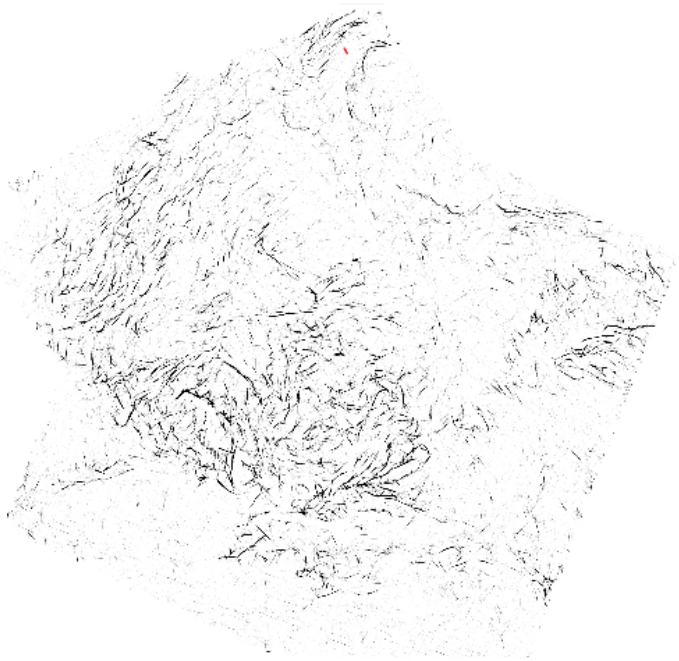

Figure 4.2: RHT visualization of the Herschel 250 μ m image of the Polaris Flare (grayscale) made with Z=0.75, Dw=41, Dk=5

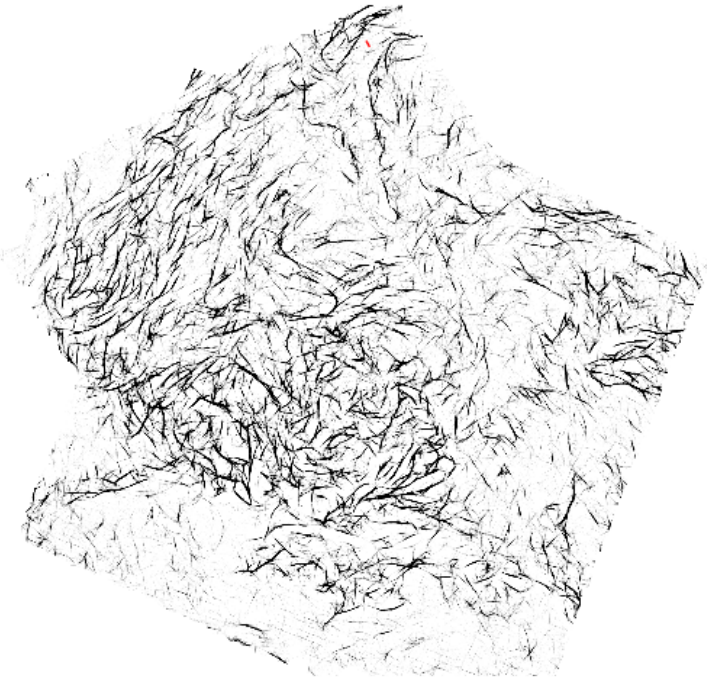

Figure 4.3: RHT visualization of the Herschel 250 μm image of the Polaris Flare (grayscale) made with Z=0.7, Dw=61, Dk=10.

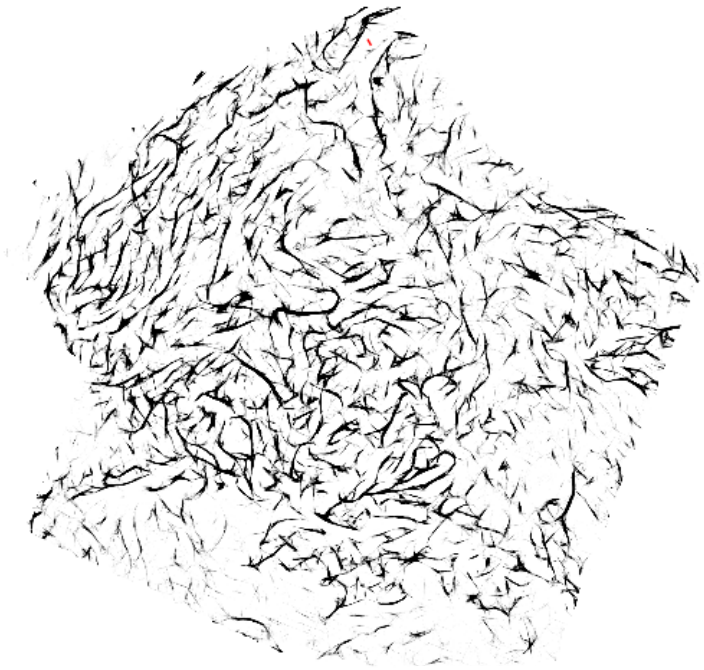

Figure 4.4: RHT visualization of the Herschel 250 μm image of the Polaris Flare (grayscale) made with Z=0.75, Dw=61, Dk=20.

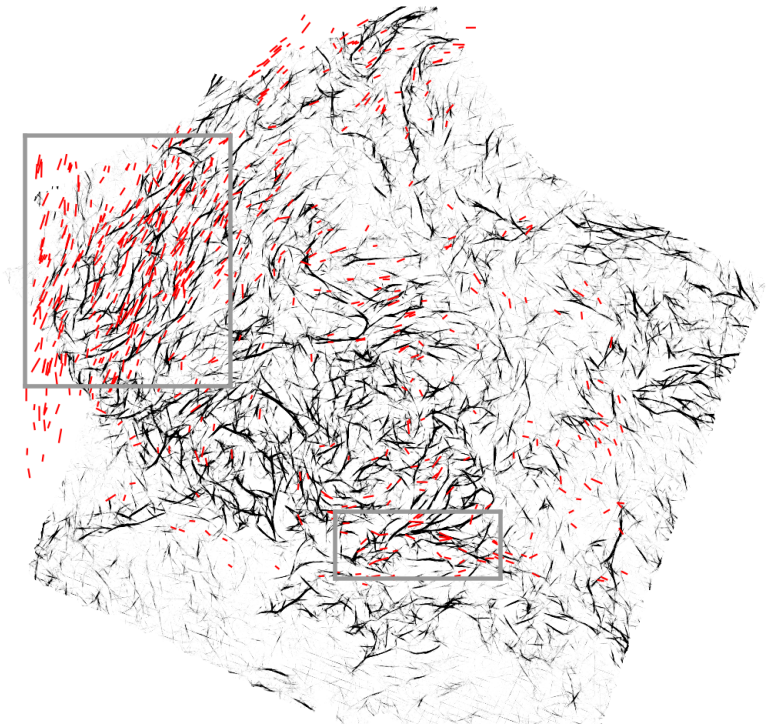

Figure 4.5: RHT visualization of the Herschel 250 μm image of the Polaris Flare (grayscale). Dark pixels correspond to a high probability of linearity.

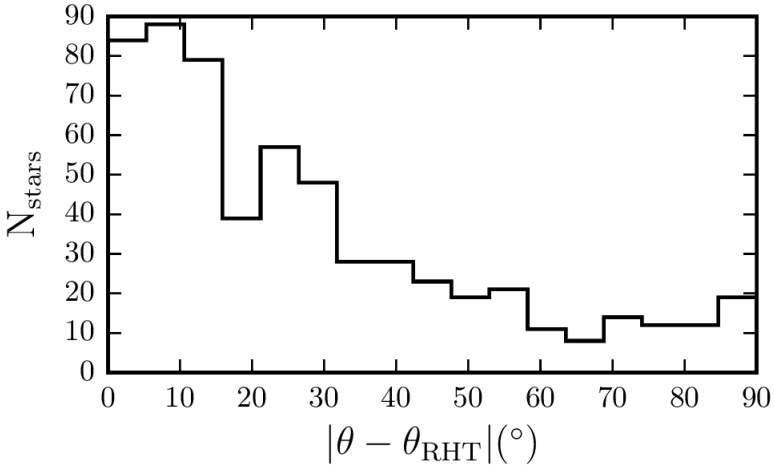

Figure 4.6: Distribution of the absolute difference between the angle of each polarization segment and the RHT angle.

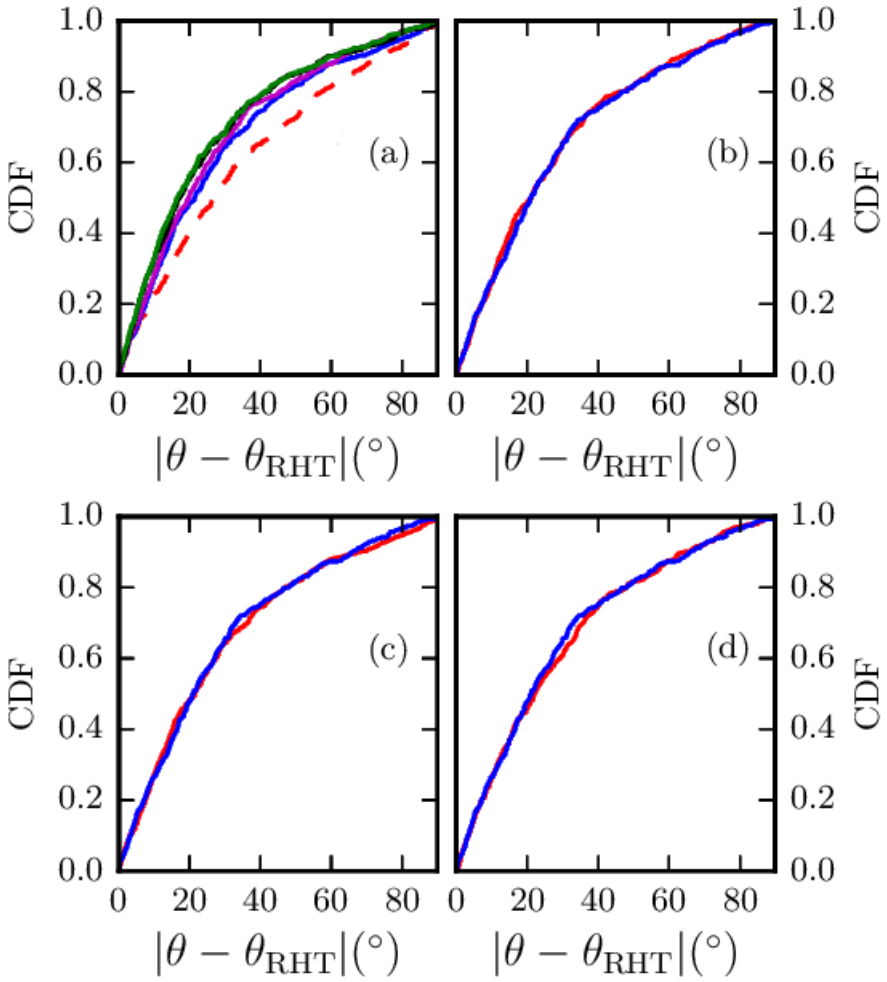

Figure 4.7: (a): CDF of different d. (b): CDF diagram of different window diameter. (c): CDF of different threshold values. (d): CDF of different smooth values.

4.3 Parameter study

We explored the effect of changing the parameters of the RHT, as well as the area around each star used in calculating $\theta_{\rm RHT}$. There are 4 parameters that we can vary while running the RHT code. The first is the diameter of the region in which the average RHT angle was computed. We vary this value from 0.04 pc to 0.16 pc (11 to 51 pixels) and plot the CDF of the resulting distributions of $\langle \theta - \theta_{RHT} \rangle$ in panel (a) of Fig.4.7. The dashed line indicates the CDF resulting from $d = 0.04$ pc. All distributions above this value $d > 0.084$ pc converge. We also varied the parameters used in running the RHT (window diameter, threshold value, smoothing diameter). The CDFs of the extreme values used in the parameter study are shown in panels (b)−(d) of Fig. 4.7. In all cases, the corresponding distributions are consistent with each other thus there is no significant variation for a large portion of the parameter space.

Chapter 5

Variations across the field

The results presented above on the alignment of filaments and B_{pos} concerned the entire map. However, both field and cloud structure are not homogeneous across the cloud. For example, there is a low column density area of striations where B_{pos} exhibits ordered structure. Adjacent to this area, towards lower latitude and longitude, in a significant portion of the map, measurements are sparse and polarization angles show substantial dispersion.

The various trends existing in the measured cloud properties can be better visualized by constructing maps of average (smoothed) quantities across the sky. The maps are constructed by creating a grid (5' squares) of the field. The value at each grid center is calculated by averaging the values of star measurements within 10' of it. The final map is smoothed using a boxcar filter of 5' width. Figure 5.1 shows such maps of various quantities: (a) number of significant stellar polarization measurements ($p_d/\sigma_p \geq 2.5$), (b) *Herschel* 250 μm intensity, (c) polarization angle, θ, (d) scatter of θ, (e) $|\theta - \theta_{\rm RHT}|$ and (f) p_d. Only bins with at least 5 measurements were used to produce the maps (reducing this number to 3 did not make a qualitative difference).

The number of significant stellar polarization measurements is highest in region A, which is the bright part in the upper left of the map in panel (a). The number density (per 5 bin) in this area is more than twice that in the rest of the map. Smaller local maxima are found: (i) in region B, (ii) in the center of the map (123.5°, +26.3°) and (iii) above the striations at (124.5°, +27.5°). This variation in the number of measurements is not due to variations in stellar density across the field, or due to systematics such as observing conditions. Panel (b) shows the *Herschel* 250 μm image smoothed with a boxcar filter of 5' width. The MCLD123 filament (region B) stands out as a maximum of intensity. By comparing the number density of significant stellar polarization measurements to the dust emission intensity (panels (a) and (b)) we find that the overall structure of the two maps is significantly different. Therefore, the variation of the density of significant polarization measurements cannot be attributed to variations in the column density.

The average polarization angles in panel (c) are calculated as the circular mean:

$$\bar{\theta} = \frac{1}{2}\arctan\left(\frac{\sum_{\rm i=1}^{\rm N}\sin(2\theta_{\rm i})}{\sum_{\rm i=1}^{\rm N}\cos(2\theta_{\rm i})}\right), \tag{5.1}$$

where N is the number of measurements in each bin. The average polarization angle defines a number of domains of different orientation throughout the field, separated by abrupt angle changes. The thin dark curves at the edges of some domains are an artefact of the smoothing, they do not represent measurements of 90°. In the largest domain, which contains region A, $\bar{\theta}$ seems to rotate clockwise from 160° (bright yellow) to 40° (blue) below the center of the map.

The scatter of polarization angles std(2θ) in panel (d) is measured using the circular standard deviation:

$$\mathrm{std}(2\theta) = \sqrt{-2\ln\left(\sqrt{\left(\frac{1}{\rm N}\sum_{\rm i=1}^{\rm N}\sin 2\theta_{\rm i}\right)^2 + \left(\frac{1}{\rm N}\sum_{\rm i=1}^{\rm N}\cos 2\theta_{\rm i}\right)^2}\right)}. \tag{5.2}$$

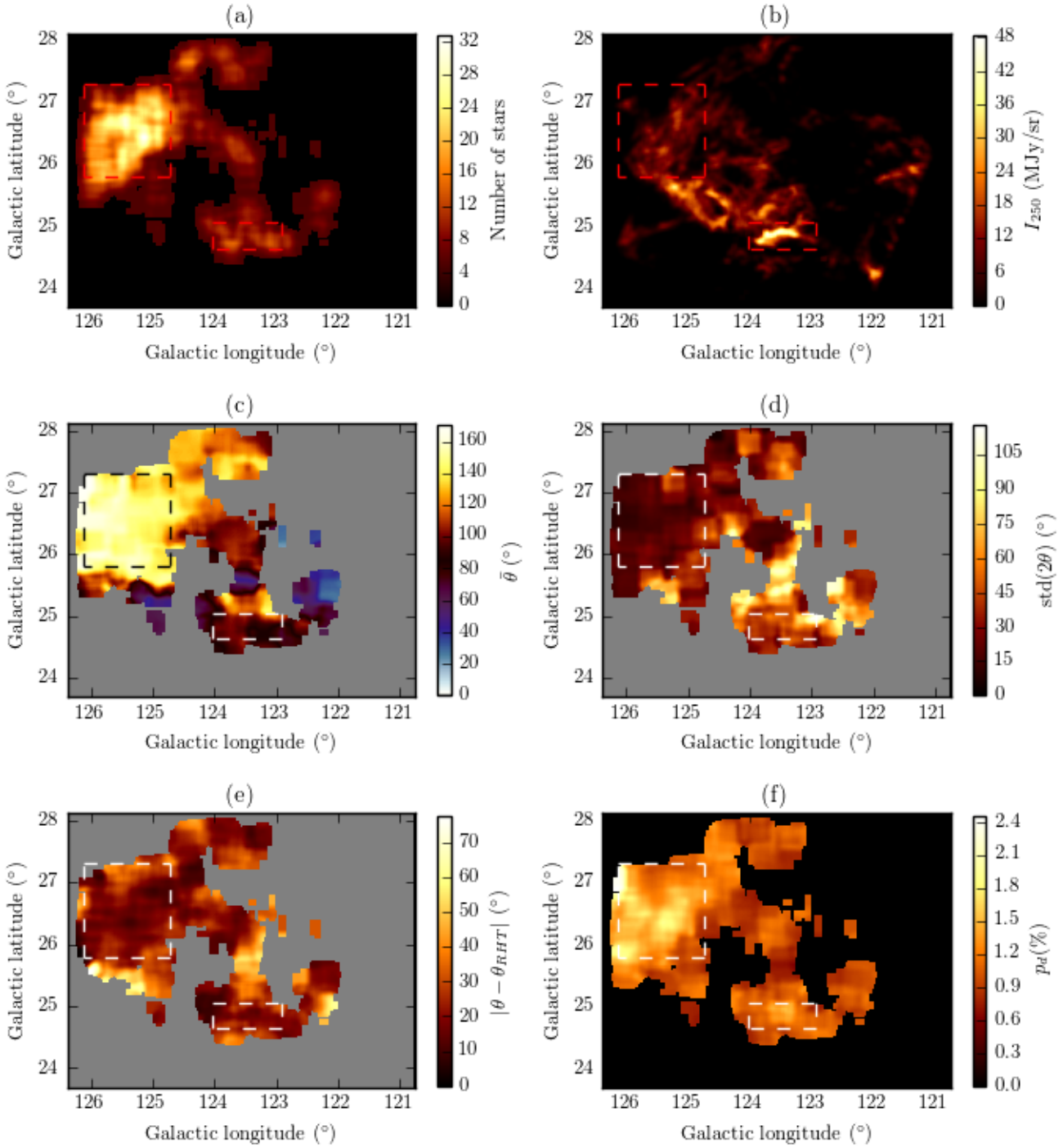

Figure 5.1: Quantities smoothed on a 5×5grid: (a) number of stellar polarization measurements, (b) *Herschel* 250 μm intensity, (c) polarization angle, (d) polarization angle scatter, (e) relative orientation of B_{pos} and filaments, (f) fractional linear polarization.

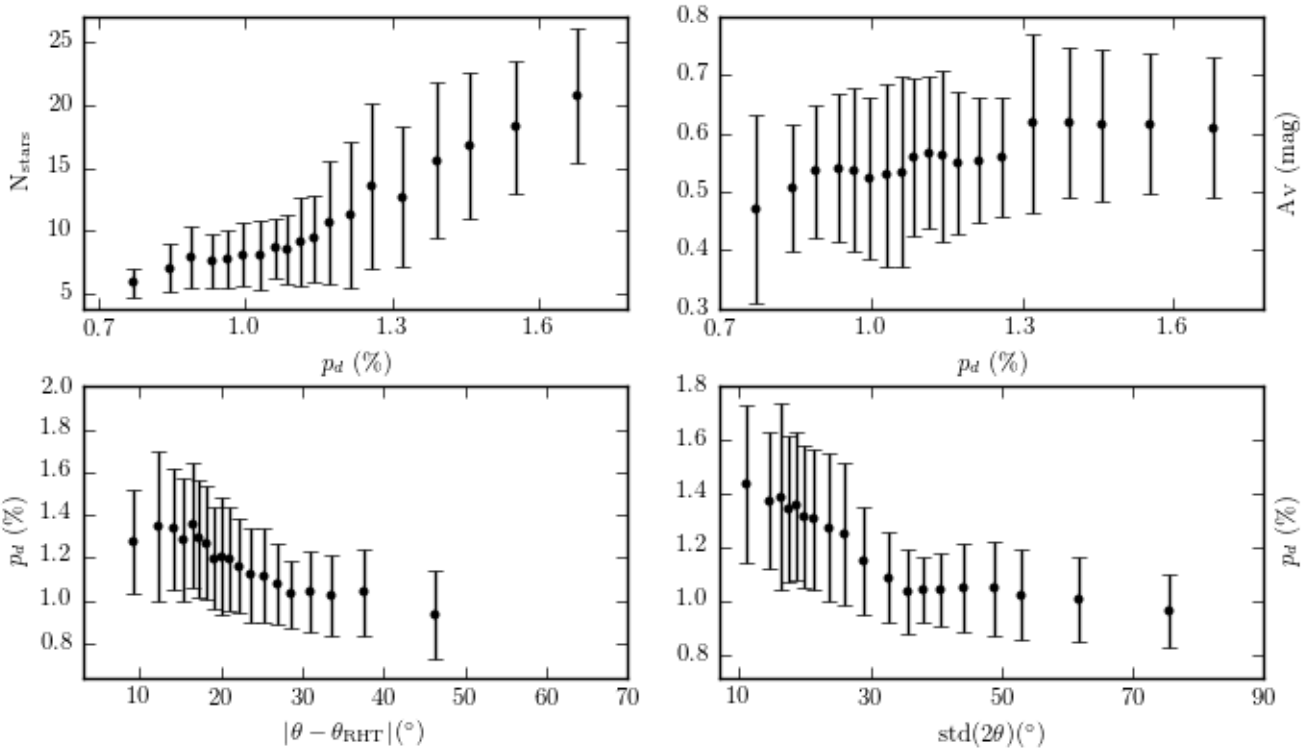

Figure 5.2: Binned pixel-to-pixel comparison of maps from Fig. 5.1. Top left: N_{stars} versus p_d, top right: extinction A_V versus p_d, bottom left: p_d versus $|\theta - \theta_{RHT}|$, bottom right: p_d versus std(θ). Errorbars show the $\pm 1\sigma$ from the mean in each bin. Bins contain the same number of pixels.

The values obtained by this equation do not represent the dispersion that would characterize a normal distribution of angles. They only serve for comparison between the various areas of the map. The bright regions in panel (d) (large standard deviations) correspond to regions with very few measurements, as can be seen by comparing with panel (a). Region A and an area with std$(2\theta) < 30^\circ$ in the center of the map stand out as the areas with lowest dispersion.

The relative orientation of B_{pos} and the filamentary structures in the cloud, shown in panel (e), is very similar to the std(2θ) map. Regions characterized by a large polarization angle dispersion appear to coincide with regions where filaments are perpendicular to B_{pos}. The preference in alignment throughout the map, seen in Fig. 4.6 , is evident, as regions with $|\theta - \theta_{RHT}| \leq 20^\circ$ (dark) occupy most of the map area. The region with the highest density of orthogonal measurements is at the top of the map.

The highest values of p_d (panel f) are in the region of the striations. The *Planck* polarized intensity peak coincides with the brightest part of this map at (126°, +27°). The second, but lower, local maximum in p_d is in region B. The spatial variation of p_d resembles that of N_{stars}. This correlation is evident in Fig. 5.2 (top left), where the average value of N_{stars} is plotted for each (equally-populated with pixels) p_d bin. This correlation is natural, since the polarization measurements were selected Panopoulou et al. [2015] to satisfy $p_d/\sigma_p \geq 2.5$. Since the observational errors σ_p are uniform across the field, it is more likely that a larger number of significant measurements will be obtained in regions of higher p_d.

Additional support to the fact that the variation in the number of significant polarization measurements is uncorrelated with the column density is given by the plot on the top right panel of Fig. 5.2, where the visual extinction, A_V, is plotted against p_d (from panel f, Fig. 5.1). One possibility that explains the observed variation of N_{stars} is that the 3D orientation of the magnetic field varies significantly throughout the sky. If this is true, then it is expected that more significant polarization will be detected in regions where the field is mostly on the plane of the sky. In these regions, p_d should be higher and this is consistent with the correlation of p_d and N_{stars} that we find.

Also, if the field strength is more significant than turbulent gas motions, which tend to randomize its orientation , regions where B_{pos} is stronger (high p_d, N_{stars}) should have a small angle scatter. This is indeed the case as can be seen in the bottom right panel of Figure 5.1. If the assumption of a strong magnetic field holds, then, diffuse, non self-gravitating filaments such as the ones in this cloud are expected to be mostly parallel to the 3D field orientation. So, if the field lies mostly on the plane of the sky, the alignment of the projected field and filaments will be easily detected. If, though, the field is mostly along the line of sight, filaments and field can be observed as having any relative orientation. This trend is evident in the bottom left panel of Figure 5.1.

The above arguments seem to indicate the presence of a strong magnetic field in the cloud which may change orientation from being mostly parallel to the plane-of-the-sky in region A to being more inclined in other areas.

Chapter 6

Filament widths

An important morphological characteristic of filaments is their width. We use the Filament Trait-Evaluated Reconstruction (FilTER) to construct the width distribution of filaments in the Herschel image. FilTER takes as input the skeleton of an image and finds the width of the elongated structures. The skeleton is produced by DisPerSe that can extract the filamentary structures of an image. It is designed to connect local maxima (cores). This property renders the construction of a representative skeleton difficult, because a significant part of the Polaris Flare does not contain bright cores. The RHT produces a visualization of filamentary structures irrespective of brightness. This enables us to apply DisPerSe to the RHT backprojection image and obtain a representative skeleton of the Herschel image to use as input to FilTER (see Figure 6.1).

The distribution of filament widths in the Herschel image is shown in Fig. 6.2. The distribution has a prominent peak at 0.06 pc and the spread of $\sigma_{\rm w} = 0.04$, twice as much as the typical error in the width determination ($\sigma_{\rm fit}$) in our implementation of the code. The intrinsic spread of the distribution is: $\sigma_{\rm int} = (\sigma_{\rm w}^2 - \sigma_{\rm fit}^2)^{1/2} = 0.035\,{\rm pc}$. Though lower than the characteristic width of 0.1 pc, the peak value found here falls within the spread of the distributions from these works.

Moreover we examine whether there are trends in the distribution of widths across the cloud, by constructing a smoothed map of the widths found by FilTER (Figure 6.3). We use a boxcar filter of the same size as the maps in Figure 5.1 (5, or 0.2 pc) to allow for a better visual comparison.

The map shows fluctuations in the width of filaments that do not appear to have any large-scale systematic trend. This remains the case for maps with smaller smoothing kernels. However, when comparing the distribution of widths within region A (Figure 6.4, left, dotted red line) to that of the rest of the map (solid black line), we find that the former is slightly shifted towards lower values. A KS (Kolmogorov-Smirnov) test rejects the hypothesis that the two originate from the same parent distribution at the 0.001 level. In constructing the distributions we discard structures with lengths less than 0.2 pc, as these have too small aspect ratios to be considered filamentary. There is an indication that the shift towards lower widths becomes more pronounced as we raise this threshold to 0.4 pc.

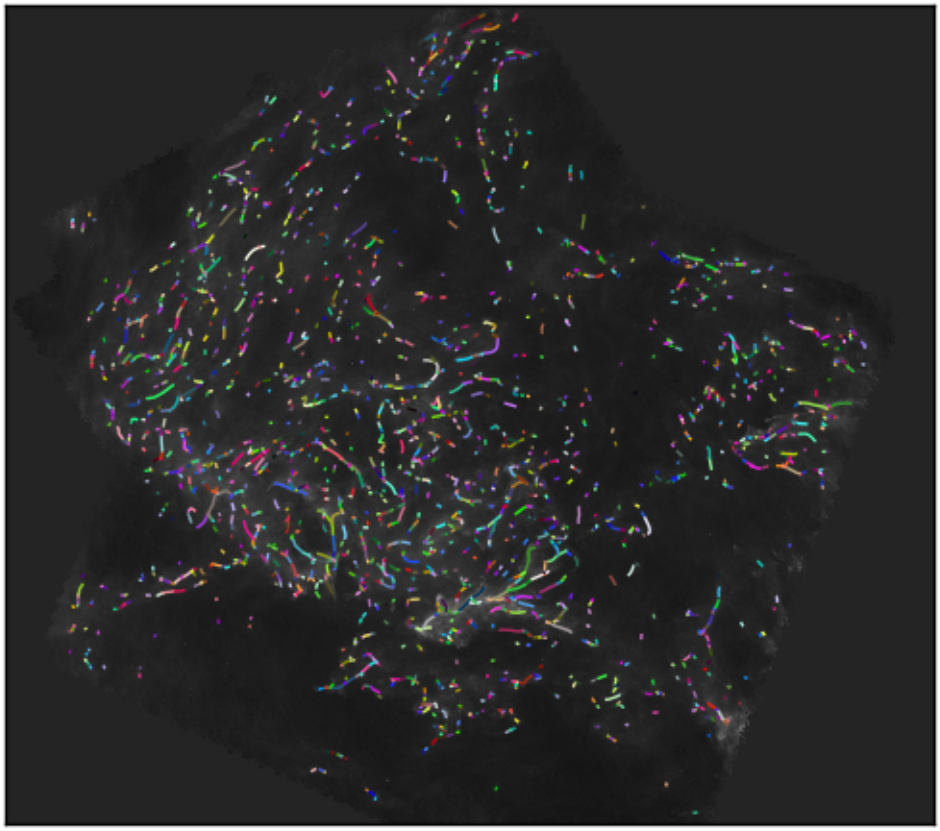

Figure 6.1: Disperse skeleton on the Herschel image of the Polaris Flare

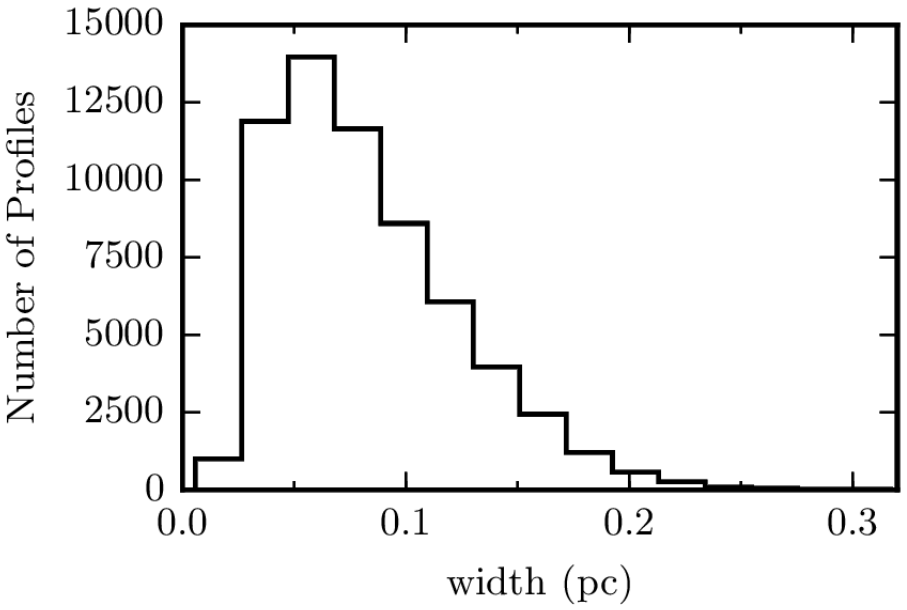

Figure 6.2: Distribution of widths along filaments in the *Herschel* image.

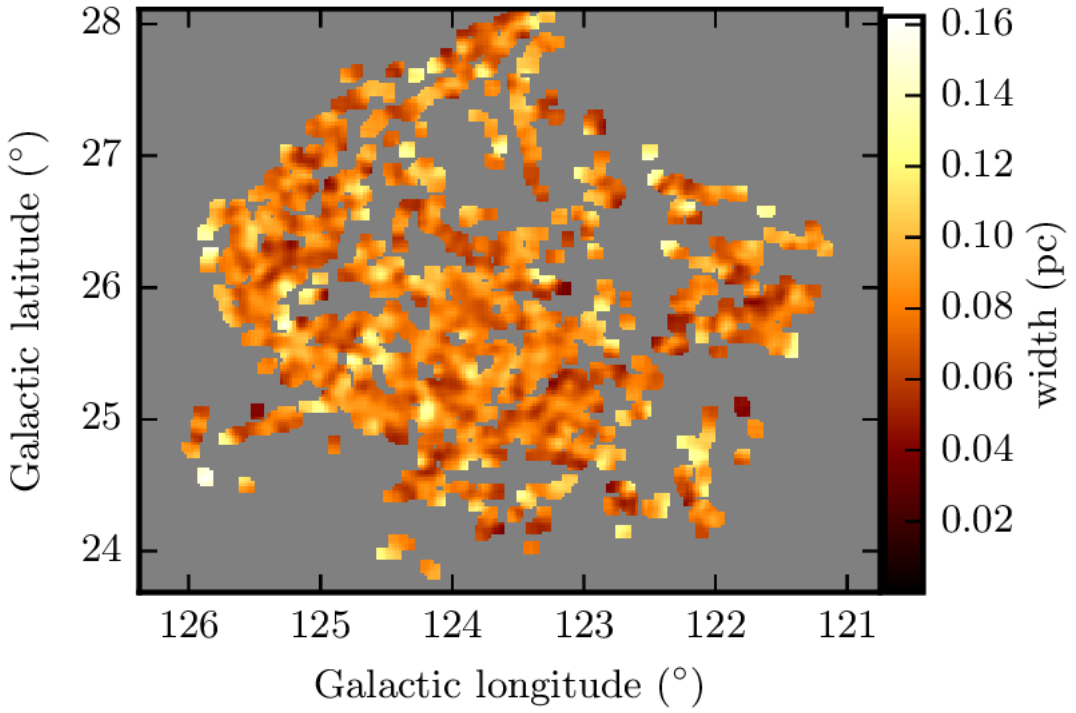

Figure 6.3: Map of filament widths found with FilTER, smoothed with a 5 arcmins boxcar filter.

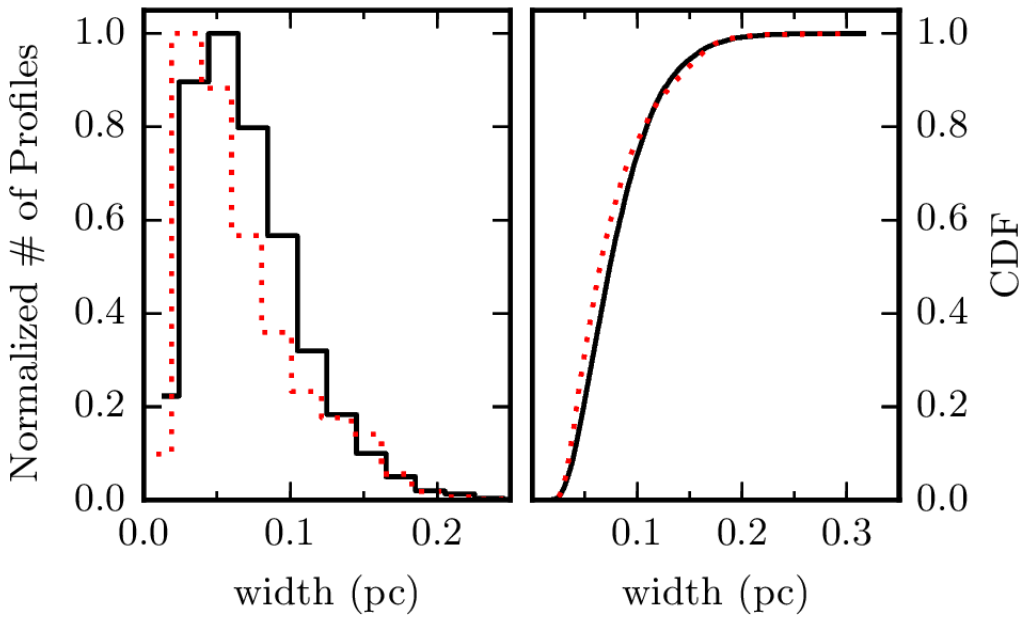

Figure 6.4: Left: Normalized distribution of widths found with FilTER in the entire map (solid black) and in region A (dotted red) for all structures longer than 0.2 pc. Right: CDF of the same distributions.

Chapter 7

Sub-regions analysis

Having explored the various observed properties of the cloud and their variation across the map, we now focus on the two regions of interest presented in Figure 7.1.

7.1 Region A

Region A contains striking features both in dust emission and in polarization. Both B_{pos} and striation orientations throughout the area are ordered. This is apparent in the distribution of polarization angles shown in panel (a) of Figure 7.2. The distribution of θ resembles a normal distribution with a mean at 153° and a standard deviation of $\delta\theta_{obs} = 11°$. The mean observational error (panel b) is 7.6° while the 80^{th} percentile of the distribution is 10°. Therefore, a significant contribution to the observed spread is due to the measurement error.

In addition to this uniformity, the mean directions of the field and dust structures appear to be aligned and this occurs to a greater extent than in the rest of the map. This is supported by the comparison of the normalized CDFs of $|\theta - \theta_{RHT}|$ shown in Figure 9, panel (c). Inside the region (dashed red line) 75% of the differences $|\theta - \theta_{RHT}|$ lie in the range [0°, 30°], whereas outside (solid black) only 57% are in the same range.

Another characteristic of region A is that it exhibits a higher fractional linear polarization than the rest of the map, as seen in panel (f) of Figure 5.1. We compare the distribution of p_d in region A (filled red) and in the rest of the map (black empty) in panel (d) of Figure 7.2. It is clear that p_d in the region extends to higher values than out of the area, and that the mean p_d (dashed line: out, dotted line: in) is lower outside the region.

7.2 Region B

Region B shows a rather different picture than region A. In this area, which is the densest part of the cloud, the plane-of-the-sky field seems to bend along the MCLD123 filament. The left panel of Figure 7.3 shows the distribution of θ for this region while the right panel shows the distribution of relative orientations, $|\theta - \theta_{RHT}|$, for region B (filled red) and the rest of the map (empty black). The distribution of θ peaks at 90°, but has a standard deviation of 25°. The spread is partly due to the large-scale curvature of B_{pos} in the vicinity and on the MCLD123 filament. The values of $|\theta - \theta_{RHT}|$ show a slight preference for alignment, although they extend to angles consistent with orthogonality.

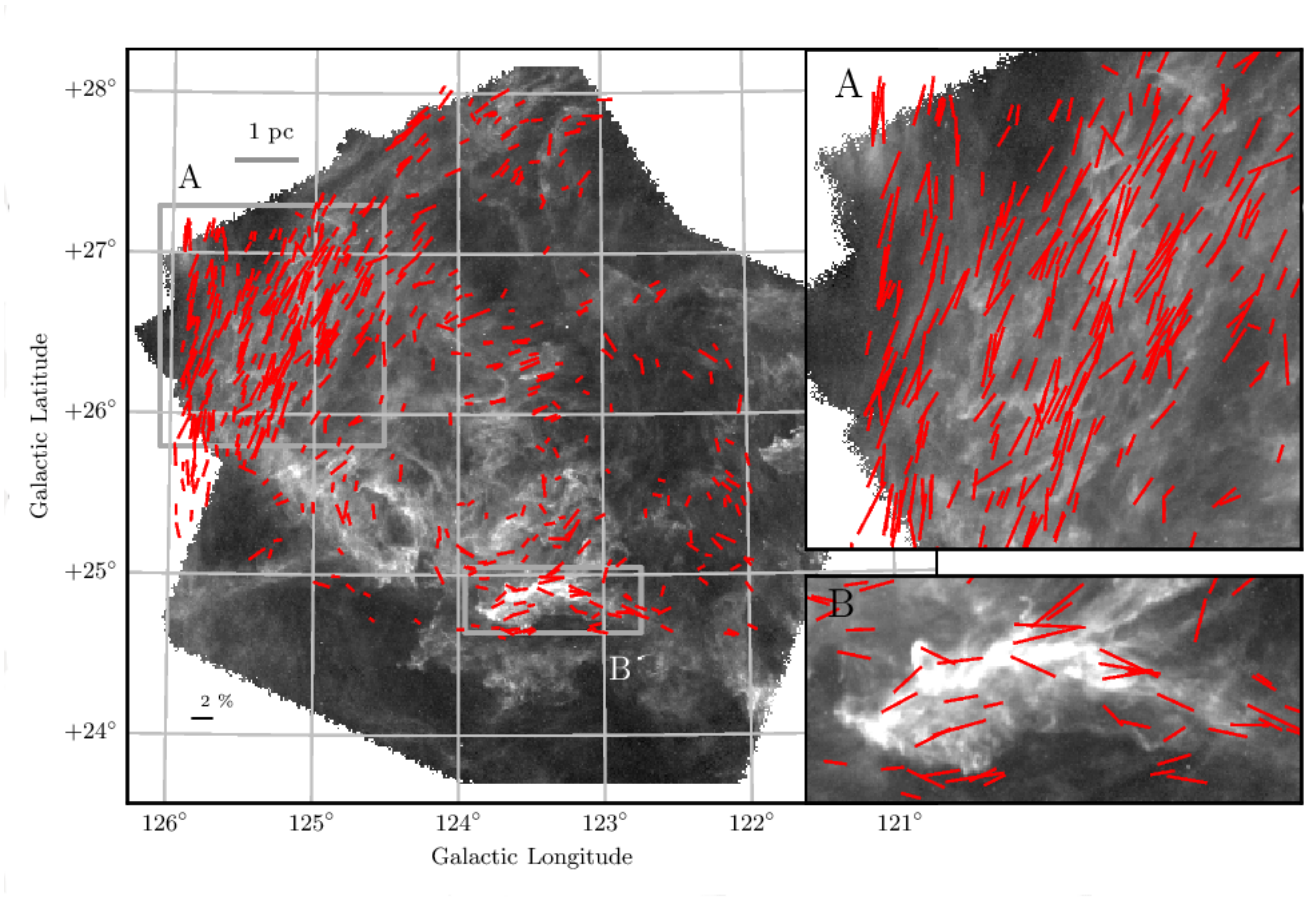

Figure 7.1: Herschel dust emission map of the Polaris Flare together with the polarization segments. Region A and Region B are shown zoomed in.

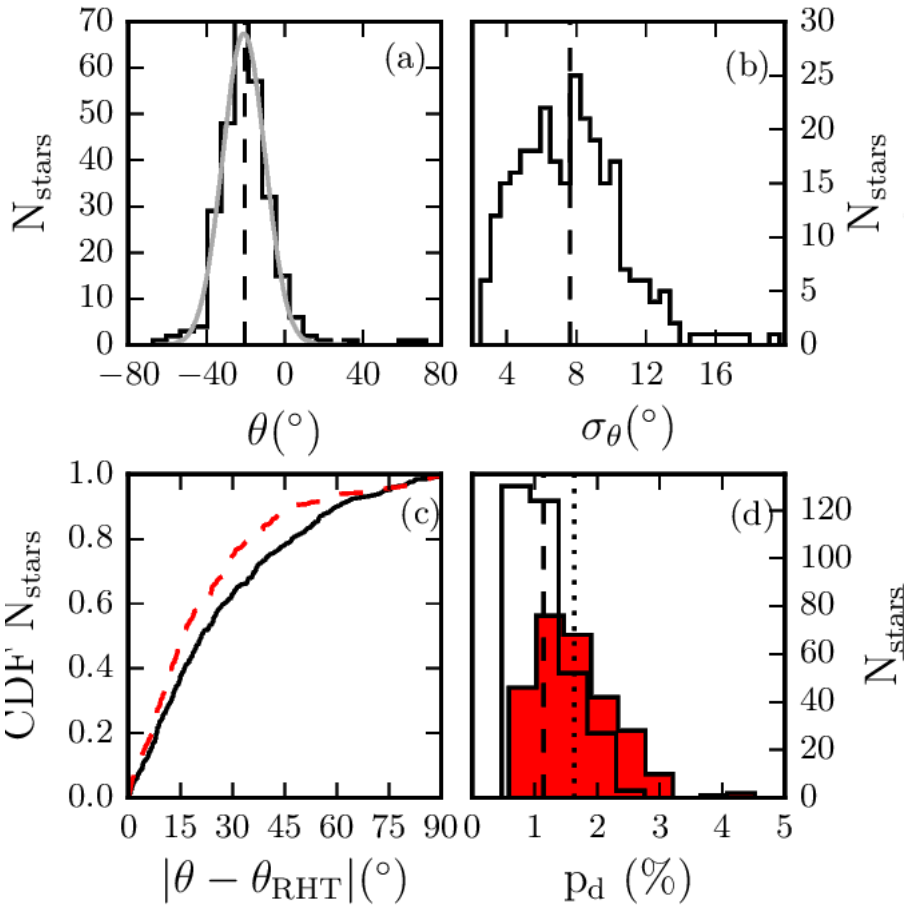

Figure 7.2: (a): Polarization angle distribution in region A (black solid), Gaussian fit (gray), average (dashed). (b) Distribution of polarization angle measurement errors in region A (solid) and mean (dashed). (c) Normalized CDFs of relative orientations of polarization measurements and dust striations in region A (dashed red) and the rest of the map (solid black). (d) Distributions of p_d in region A (filled red) and the rest of the map (empty black), dashed and dotted lines are their average values.

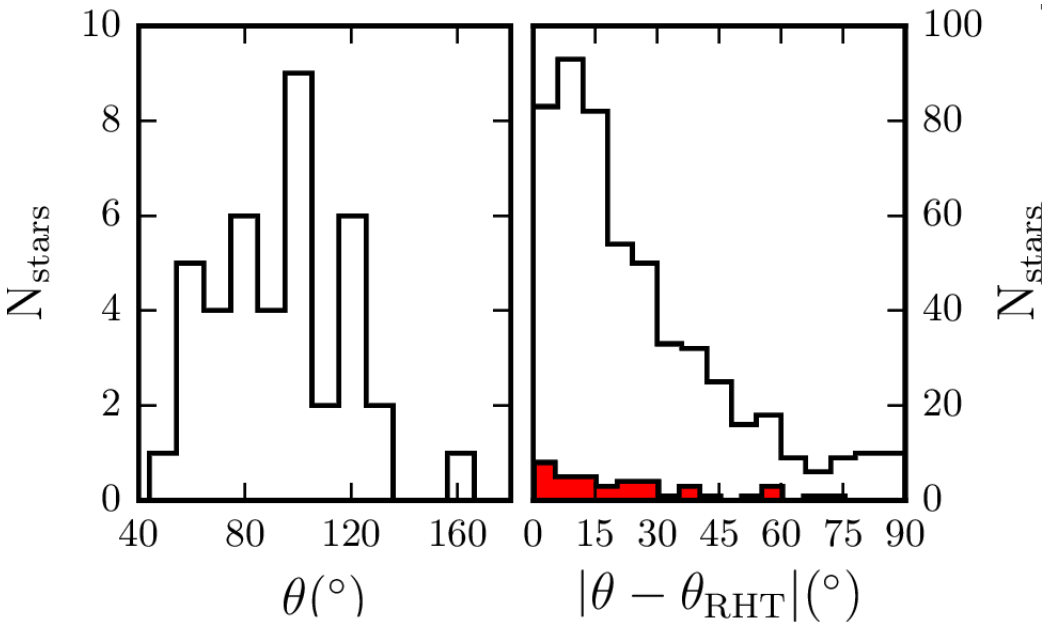

Figure 7.3: Left: distribution of polarization angles in region B. Right: distribution of $|\theta - \theta_{RHT}|$ for region B (filled red) and the rest of the map (empty black).

Chapter 8

Discussion

In this work we examine the role of the magnetic field in the Polaris Flare cloud structure and dynamics. The main results are the following. Firstly we combined the high-resolution Herschel dust emission data with the polarization data from RoboPol. We found that the elongated dust structures (filaments and striations) are well aligned with the plane-of-sky magnetic field. This alignment is more prominent in regions where the fractional linear polarization is high (and the number of significant polarization measurements is large). We noticed that the projected magnetic field of the cloud presents a very inhomogeneous structure. There are regions where it is uniform and others where the measured orientations appear random, or significant measurements are entirely absent. These characteristics may provide hints on the nature of the 3D field. Let us consider region A, which has the largest density of significant polarization measurements. This is not due to variation in stellar density, observing conditions or other systematics. Therefore, region A must be characterized by higher polarization efficiency.

The increased polarization efficiency of region A could be the result of:

i) increased alignment efficiency (e.g. more background radiation, a larger amount of asymmetric dust grains, larger grain sizes),

ii) more uniform magnetic field along the line-of-sight,

iii) increased $\mathrm{B_{pos}}$.

Additionally, the alignment of the linear structures with the ordered magnetic indicates that turbulence is sub-Alfvenic and the magnetic field is dynamically important. This claim is also supported by additional work presented in Panopoulou et al. [2016]. In this work we estimated the strength of the plane-of-the-sky field and the ratio of turbulent-to-ordered field components in two regions of the cloud: one containing diffuse striations, and the other harbouring the highest column density filament. Polarization measurements can be used to estimate the strength of $\mathrm{B_{pos}}$ under the assumption that the polarization angle dispersion ($\delta\theta$) is caused by the action of hydromagnetic waves perpendicular to the (mean) magnetic field, Davis [1951], Chandrasekhar & Fermi [1953]. Based on the idea that a strong field will resist distortion and therefore, $\delta\theta$ will be small, DCF derive:

$$\mathrm{B_{pos}} \approx \sqrt{4\pi\rho}\frac{\delta v}{\delta\theta}, \tag{8.1}$$

where ρ is the volume mass density of the gas and δv is the velocity dispersion perpendicular to the observed field (along the line-of-sight). The last quantity, $\delta\theta$, can be expressed as the ratio of the (root-mean-squared) turbulent component of the magnetic field ($\left\langle \mathrm{B_t^2} \right\rangle^{1/2}$) to the ordered component ($\mathrm{B_0}$)[Hildebrand et al. , 2009]:

$$\delta\theta \approx \frac{\left\langle \mathrm{B_t^2} \right\rangle^{1/2}}{\mathrm{B_0}}. \tag{8.2}$$

The results indicate that the ordered component of the magnetic field is larger than the turbulent component and the magnetic field is dynamically important in both regions.

Summary

We combined RoboPol optical polarization measurements and Herschel dust emission data to infer the magnetic field properties of the Polaris Flare. We found that linear dust structures (filaments and striations) are preferentially aligned with the projected magnetic field. This alignment is more prominent in regions where the fractional linear polarization is highest (and the number of significant polarization measurements is largest). This correlation supports the idea that variations in the alignment are partly caused by the projection of the 3-dimensional magnetic field. We investigated the possibility of important spatial variations in the filament widths and found only a slight indication of such an effect. Using the Davis (1951); Chandrasekhar & Fermi (1953) and Hildebrand et al. (2009) methods, we estimated the strength of the plane-of-the-sky field and the ratio of turbulent-to-ordered field components in two regions of the cloud: one containing diffuse striations, and the other harbouring the highest column density filament. Our results indicate that the magnetic field is dynamically important in both regions.

Bibliography

Andersson B.-G., Lazarian A., Vaillancourt J. E., 2015, ARAA, 53, 501

André P., Di Francesco J., Ward-Thompson D., Inutsuka S.-I., Pudritz R. E., Pineda J. E, 2014, Protostars and Planets VI, 27

André P., 2013, Highlights of Astronomy, 16

André P. et al., 2010, A&A, 518, L102

Arzoumanian D. et al., 2011, A&A, 529, L6A

Alves F. O., Franco G. A. P., Girart J. M., 2008, A&A, 486, 13A

Alves de Oliveira C., 2014, A&A, 568, 98A

Barnes P., Li D., Telesco C, Tanakul N., Marinas N., Wright C., Packham C., Pantin E., Roche P., Hough J., 2015, MNRAS, 453, 2622

Bensch F., Leuenhagen U., Stutzki J., Schieder R., 2003, ApJ, 591, 1013

Bohlin R. C., Savage B. D., Drake J. F., 1978, ApJ, 224, 132

Brunt C. M., Heyer M. H., Vázquez-Semadeni E., Pichardo B., 2003, ApJ, 595, 824B

Cambrésy L., Boulanger F., Lagache G., Stepnik B., 2001, A&A, 375, 999

Chandrasekhar S., Fermi E., 1953, ApJ, 118, 113

Chapman N. L., Goldsmith P. F., Pineda J. L., Clemens D. P., Li D., Krčo M., 2011, ApJ, 741, 21C

Clark S. E., Peek J. E. G., Putman M. E., 2014, ApJ, 789, 82

Crutcher R. M., Nutter D. J., Ward-Thompson D., Kirk J. M., 2004, ApJ, 600, 279

Dame T. M., Hartmann D., Thaddeus P., 2001, ApJ, 547, 792

Davis, Jr., L. 1951, Phys. Rev., 81, 890

Falceta-Gonçalves D., Lazarian A., Kowal G., 2008, ApJ, 679, 537

Fiege J. D., Pudritz R. E., 2000, ApJ, 544, 830

Franco G. A. P., Alves F. O., Girart J. M., 2010, ApJ, 723, 146

Franco G. A. P., Alves F. O., 2015, ApJ, 807, 5

Gillmon K., Shull J. M., 2006, ApJ, 636, 908

Girart J. M., Rao R., Marrone D. P., 2006, Science, 313, 5788, 812

Goldsmith P. F. Heyer M., Narayanan G., Snell R., Li D., Brunt C., 2008, ApJ, 680, 428

Goldsmith P. F., 2013, ApJ, 774, 134

Goodman A. A., Bastien P., Menard F., Myers P. C., 1990, ApJ, 359, 363

Gorbikov E., Brosch N., 2014, MNRAS, 443, 725

Greenberg J. M., 1968, Stars & Stellar Systems, 7, 221

Grossmann V., Heithausen A., Meyerdierks H., Mebold U., 1990, A&A, 240, 400

red Hall J. S., 1955, Liege Symposium, 543

Heiles C., 2000, AJ, 119, 923H

Heithausen A., Thaddeus P., 1990, ApJL, 353, L49

Heithausen A., Stacy J. G., de Vries H. W., Mebold U., Thaddeus P., 1993, A&A, 268, 265

Heithausen A., 1999, A&A, 349, L53

Heitsch F., Zweibel E. G., Mac Low M.-M., Li P., Norman M. L., 2001, ApJ, 561, 800

Hennebelle P., 2013, AA, 556, A153

Hildebrand R. H., Kirby L., Dotson J. L., Houde M., Vaillancourt, J. E., 2009, ApJ, 696, 567

Hily-Blant P., Falgarone E., 2007, A&A, 469, 173

Hily-Blant P., Falgarone E., 2009, A&A, 500, L29

Houde M., Vaillancourt J. E., Hildebrand R. H., Chitsazzadeh S., Kirby L., 2009, ApJ, 706, 1504

Keenan P. C., Babcock H. W., 1941, ApJ, 93, 64K

Koch E. W., Rosolowsky E. W., 2015, MNRAS, 452, 3435

red Lee H. M., Draine B. T. 1985, ApJ, 290, 211

Li H.-B., Fang M., Henning T., Kainulainen J. 2013, MNRAS, 436, 3707

Malinen J. et al., 2015, MNRAS submitted, arXiv:1512.03775

Matthews B. C., Wilson C. D., Fiege J. D., 2001, ApJ, 562, 400

Men'shchikov A. et al.,2010, A&A, 518, L103

Miville-Deschênes M.-A. et al., 2010, A&A, 518, L104

Mouschovias T. C., 1976, ApJ, 206, 753

Mouschovias T. C., 1991

Myers P. C., 2009, ApJ, 700, 1609

Nakamura F., & Li Z.-Y., 2008, ApJ, 687, 354

Ostriker E. C., Stone J. M., Gammie C. F., 2001, ApJ, 546, 980

Padoan P., Goodman A. A., Draine B. T., Juvela M., Nordland Å. R, Rögnvaldsson O. E., 2001, ApJ, 559, 1005

Palmeirim P. et al., 2013, A&A, 550A, 38P

Panopoulou G. V., Tassis K., Goldsmith P. F., Heyer M., 2014, MNRAS, 444, 2507P

Panopoulou G. V. et al., 2015, MNRAS, 452, 715

Panopoulou G.V., Psaradaki I., Tassis K., 2016, MNRAS

Pereyra A., Magalhães A. M., 2004, ApJ, 603, 584

Pilbratt G. L. et al., 2010, A&A, 518, L1

Planck Collaboration et al., 2015, A&A, 576, 104

Planck Collaboration et al., 2015, A&A, 576, 105

Planck Collaboration et al., 2014, A&A, in press, arXiv:1409.6728

Planck Collaboration et al., 2015, preprint, (arXiv:1502.04123)

Savage B. D., Mathis J. S., 1979, ARA&A, 17, 73S

Schlafly E. F. et al., 2014, ApJ, 786, 29S

Schlegel D. J., Finkbeiner D. P., Davis M., 1998, ApJ, 500, 525

Schneider N. et al., 2013, ApJL, 766, L17

Soler J. D., Hennebelle P., Martin P. G. et al., 2013, ApJ, 774, 128

Sousbie T., 2011, MNRAS, 414, 350

Sugitani K. et al., 2011, ApJ, 734, 63S

Tassis K., 2014, Hipparchus

van den Bergh, S., 1956, Z. Ap., 40, 249

Wagle G. A., Troland T. H., Ferland G. J., Abel N. P., 2015, ApJ, 809, 17W

Ward-Thompson D. et al., 2010, A&A, 518, L92

Weinkauf and D. Gunther, Separatrix persistence: Extraction of salient edges on surfaces using topological methods. Computer Graphics Forum (Proc. SGP '09), 28(5):1519–1528, July 2009]

Zagury F., Boulanger F., Banchet V., 1999, A&A, 352, 645